



**UiT** The Arctic University of Norway

Faculty of Science and Technology  
Department of Physics and Technology

## **Investigating the Impact of Susceptibility Artifacts on Adjacent Tumors in PET/MRI through Simulated Tomography Experiments**

Erlend Bredal Olsen

FYS-3941 Master's thesis in applied physics and mathematics 30 SP

This thesis document was typeset using the *UiT Thesis L<sup>A</sup>T<sub>E</sub>X Template*.

© 2021 – <http://github.com/egraff/uit-thesis>

# Abstract

For quantitative PET imaging, attenuation correction (AC) is mandatory. Currently, all main vendors of hybrid PET/MRI systems apply a segmentation-based approach to compute a Dixon AC-map based on fat and water images derived from in- and opposed-phase MR-images. Changes in magnetic susceptibility pose major problems for MRI, which may lead to artifacts resulting in tissue misclassification in the segmented AC-map. Cases have been reported where the liver has been misidentified as lung tissue due to iron overload, e.g. from hemochromatosis or iron oxide MR contrast agents, resulting in severe underestimation of PET-quantification.

In this thesis, simulated tomography experiments were conducted to investigate the impact of susceptibility artifacts on adjacent tumors, focusing on the misclassification of liver tissue as lung tissue. A digital phantom was programmed, and synthetic tumors and artifacts were introduced into a realistic PET/MRI patient dataset. The data were reconstructed with attenuation maps both with and without artifacts to compute the relative error ( $RE$ ) in tumor uptake.

It was shown that relevant errors can be introduced to tumors adjacent to the artifact. A strong inverse square relationship between the distance ( $d$ ) of the center points of a tumor and an artifact was found with the  $RE$ . Further, because the  $RE$  was known to be proportional to the volume ( $V$ ) of misclassified tissue, it was shown that it is possible to obtain a linear equation describing the  $RE$  using only  $V$  and  $d$ . However, this assumes similar information, i.e activity and attenuation, along the common line of responses (LORs) of the artifact and tumor.

A correction method was developed to correct for lung-liver misclassifications. The proposed method uses the already acquired opposed-phase Dixon images, which are less sensitive to susceptibility changes. It successfully corrected 96% of misclassified tissue down to a 50% MR-signal reduction from the liver. The method benefits from using already acquired data to correct the artifacts, and may be made fully automatic to function in real-time.



# Acknowledgements

I would like to send a big thanks to my supervisors, Ola Engelsen and Svein Jacobsen for their help and guidance. A special thank you to Kent Johansen for acquiring the PET/MRI patient dataset, and to Ola for handling the data protection formalities so that I could access the patient image data. Also, thank you to PET/MRI radiologist Miguel Castillejo for introduction to the problem of MR-signal loss from liver iron overload. To the people of the PET center at the University Hospital of Northern Norway (UNN); thank you for letting me occupy your space through the last year!

Thank you to my family for your support, and last, but not least: Thank you Vilde, my soon-to-be wife, for your patience and support, and for being my motivation.

*Erlend Bredal Olsen*  
Tromsø, May 2021



# Contents

<b>Abstract</b>	<b>i</b>
<b>Acknowledgements</b>	<b>iii</b>
<b>List of Figures</b>	<b>vii</b>
<b>List of Tables</b>	<b>ix</b>
<b>Abbreviations</b>	<b>xi</b>
<b>1 Introduction</b>	<b>1</b>
1.1 Motivation and objective . . . . .	1
<b>2 Theory</b>	<b>5</b>
2.1 Basic MRI . . . . .	5
2.1.1 Physics of MRI . . . . .	5
2.1.2 Contrast in MRI . . . . .	10
2.1.3 Dixon method . . . . .	12
2.2 Basic PET . . . . .	14
2.2.1 Physics of PET . . . . .	14
2.2.2 PET image formation . . . . .	16
2.2.3 Image reconstruction . . . . .	20
2.2.4 Attenuation correction . . . . .	21
2.2.5 The mathematics of attenuation correction . . . . .	22
2.3 Hybrid PET/MRI systems . . . . .	24
2.3.1 MRAC on the Siemens Biograph mMR . . . . .	25
2.4 Image processing . . . . .	26
2.4.1 Image segmentation . . . . .	26
2.5 Statistical analysis . . . . .	29
2.5.1 Linear regression . . . . .	30
<b>3 Materials and methods</b>	<b>33</b>
3.1 Artifact impact on adjacent tumors . . . . .	33

3.1.1	Acquiring emission data and attenuation maps for re- construction . . . . .	34
3.1.2	Creation of a digital phantom . . . . .	36
3.1.3	Setups of the digital phantom . . . . .	37
3.1.4	Simulating tumors and artifacts in a patient dataset . . . . .	38
3.2	Correction method for lung-liver misclassifications . . . . .	42
3.2.1	Correction algorithm . . . . .	43
<b>4</b>	<b>Results</b>	<b>47</b>
4.1	Artifact impact on adjacent tumors . . . . .	47
4.1.1	Effect of tumor distance to artifacts in segmented MRAC images . . . . .	47
4.1.2	Effect of tumor activity . . . . .	57
4.2	Performance of correction method . . . . .	62
<b>5</b>	<b>Discussion</b>	<b>65</b>
5.1	Misclassifications in segmented MRAC . . . . .	65
5.2	Correction method . . . . .	69
5.3	Summary . . . . .	70
<b>6</b>	<b>Conclusion</b>	<b>73</b>
<b>A</b>	<b>Appendix</b>	<b>79</b>
A.1	Patient dataset . . . . .	79
A.2	Python code for running simulated tomography experiments and reconstructions . . . . .	79
A.2.1	Class for simulating tomography experiments and do reconstruction . . . . .	80
A.2.2	Class for activity maps . . . . .	83
A.2.3	Class for attenuation maps . . . . .	86
A.3	Python code for correction method . . . . .	87



# List of Figures

2.1	Illustration of a proton's precession due to an external magnetic field [25]. . . . .	6
2.2	Schematic representation of the basic principles of MRI [26].	8
2.3	Schematic representation of $T_1$ relaxation [26]. . . . .	9
2.4	Schematic representation of $T_2$ relaxation [26]. . . . .	9
2.5	Figure shows that fat and water protons precess at different frequencies. Their phases completely cancel at TE of 2.2 msec (opposed-phase), and are additive at TE of 4.4 msec (in phase) [28]. . . . .	13
2.6	Illustration of the four main coincidence event types [29, p. 36]. . . . .	18
2.7	Schematic drawing of a PET scanner of ring geometry. [29, p. 8]. . . . .	18
2.8	Illustration of the formation of a sinogram [30, p. 179]. . . .	20
2.9	Effect of AC on a cylinder with uniform activity distribution [29, p. 57] . . . . .	21
2.10	Illustration of the parameterization to polar coordinates. [34]	23
2.11	Illustration of a hybrid PET/MRI system [2, p. 244] . . . . .	25
2.12	Illustration of intensity histograms that can be partitioned by (left) single threshold and (right) multiple thresholds. [36, p. 743] . . . . .	27
3.1	Illustration of 2-D slice for $\lambda^*$ , $\mu$ and $\mu_{art}$ for the digital phantom. TBR = 4. . . . .	36
3.2	Noise free phantom setup. . . . .	38
3.3	Figure of the activity map (left) and attenuation map (right) of the selected slice from patient for analysis. . . . .	39
3.4	Illustration of placement of tumors and artifact where the artifact diameter is 1.0 cm. Tumors placed along a line. . . . .	40
3.5	Illustration of placement of tumors and artifact where the artifact diameter is 8.3 cm. . . . .	40
3.6	Illustration of placement of tumors and artifact where tumors have been randomly placed. . . . .	41

3.7	The workspace in 3D Slicer showing the segmentation of the liver. The top image shows the whole 3D segmentation and the bottom row an axial (left), coronal (middle) and saggital (right) slice. . . . .	43
3.8	Coronal slice of original attenuation map (left) and the same slice where the artifact has been introduced (right). . . . .	44
3.9	Illustration of opposed-phased images with different liver signal intensities. . . . .	45
4.1	$RE$ vs. $d$ for the digital phantom experiment. . . . .	48
4.2	$RE$ vs. $d^{-2}$ for the digital phantom experiment. . . . .	49
4.3	$RE$ vs. $V/d^2$ for the digital phantom experiment. . . . .	50
4.4	$RE$ vs. $d$ for the patient dataset. Tumor placed along line. . .	51
4.5	$RE$ vs. $d^{-2}$ for the patient dataset. Tumor placed along line. .	52
4.6	$RE$ vs. $V/d^2$ for the patient dataset. Tumor placed along line. .	53
4.7	$RE$ vs. $d$ for the patient dataset. Random placement of tumors. .	54
4.8	$RE$ vs. $d^{-2}$ for the patient dataset. Random placement of tumors. .	55
4.9	$RE$ vs. $V/d^2$ for the patient dataset. Random placement of tumors. . . . .	56
4.10	Contour plot of the relative error overlayed on $\lambda^*$ (left) and $\mu_{art}$ (right) . . . . .	57
4.11	Illustration of the error of phantom reconstructions with TBR=1.5	58
4.12	Illustration of the error of phantom reconstructions with TBR=2	59
4.13	Illustration of the error of phantom reconstructions with TBR=4	60
4.14	Illustration of the error of phantom reconstructions with TBR=8	61
4.15	Histograms for intensity values of voxels. . . . .	62
4.16	Performance of correction method illustrated for the same coronal slice as in figure 3.8. . . . .	64

# List of Tables

2.1	Linear attenuation coefficients for different tissue types [8, p. 56]. . . . .	16
4.1	Parameters measuring the goodness of fit for regression lines in figure 4.2. . . . .	49
4.2	Tabulated values of $RE$ [%] observed in figure 4.4. Any $RE \leq \Delta_{sig}$ is marked with an asterisk. . . . .	52
4.3	Parameters measuring the goodness of fit for regression lines in figure 4.5. . . . .	53
4.4	Tabulated values of $RE$ s observed in figure 4.7. Any $RE \leq \Delta_{sig}$ is marked with an asterisk. . . . .	54
4.5	Parameters measuring the goodness of fit for regression lines in figure 4.8. . . . .	55
4.6	Performance of correction method for different liver signal intensities in the opposed-phase images. . . . .	63



# Abbreviations

**AC** attenuation correction

**APD** avalanche photodiodes

**EM** expectation maximization

**FID** free induction decay

**FOV** field of view

**FWHM** full width at half maximum

**HU** Hounsfield units

**LAC** linear attenuation coefficient

**LOR** line of response

**ML** maximum likelihood

**MLEM** maximum likelihood expectation maximization

**MR** magnetic resonance

**MRAC** MRI-based attenuation correction

**MRI** magnetic resonance imaging

**NMR** nuclear magnetic resonance

**OSEM** ordered subsets expectation maximization

**PD** proton density

**PET** positron emission tomography

**PET/CT** combined PET and CT

**PET/MRI** combined PET and MRI

**PMT** photo-multiplier tube

**RE** relative error

**RMSE** root mean squared error

**TBR** tumor-to-background ratio

**TE** echo time

**TOF** time of flight

**TR** repetition time

**UTE** ultra-short echo time

**VOI** volume of interest



# Introduction

## 1.1 Motivation and objective

Hybrid positron emission tomography (PET) and magnetic resonance imaging (MRI) systems have over the last decade proven to be highly successful in both pre-clinical and clinical applications. Particularly, when it comes to leveraging the very sensitive functional information of PET together with the superb soft tissue contrast and high-resolution structural and anatomical information from MRI. For both neurological and abdominal imaging, this makes MRI the preferred imaging modality to CT [1]. Another motivation for the fusion of the two modalities is the significantly lowered radiation dose compared to PET/CT, which could be particularly important for pediatric imaging, or for patients requiring multiple consecutive scans [2, 3]. Besides the tasks of cancer detection and staging, PET/MRI imaging is also becoming more important as a quantitative indicator for individual treatment planning or response evaluation for therapy [4].

Apart from the technical challenges that had to be overcome to successfully integrate PET systems into MRI [5], methods of accurate attenuation correction (AC) have been, and still are, the most challenging issue of hybrid PET/MRI imaging [6, 7]. AC is mandatory to provide a valid quantification of the distribution of radioactivity in the human body, and when implementing MR-based AC-methods, several aspects must be considered. Because image contrast in MRI depends on tissue relaxation times and proton density, rather than electron density which is relevant for the attenuation of 511 keV annihilation photons, it

is not possible to obtain a direct mapping of MR-signals to photon attenuation values. This also means that some tissue types, e.g. bone and lung tissue, are difficult to visualize given the low proton density of these substances.

All main vendors of clinically available PET/MRI systems today have chosen a segmentation-based approach for MRI-based attenuation correction (MRAC) [8]. Segmentation-based MRAC involves acquisition of a predefined MRI sequence and a subsequent series of post-processing steps to segment the image into different tissue classes, where each voxel is assigned an *a priori* attenuation coefficient according to the tissue class it belongs to. Apart from the well known MRAC problems, such as the difficulty to represent bone or the limited transaxial field of view (FOV) of MRI systems, susceptibility problems pose major problems for MRI and thus MRAC. Susceptibility artifacts can be subtle, and typically show up as regions of lowered or zero intensity in the image [9, p. 101].

Several cases have reported misclassification of liver tissue as lung tissue which resulted in severe underestimation of radiotracer uptake in the liver [10, 11, 12]. Because the liver is a major site for iron storage in the body [13] this organ is especially exposed for these kinds of susceptibility artifacts, and therefore segmentation errors in the MRAC. This is due to the strong magnetic properties of iron. Hemochromatosis [11, 10] and several superparamagnetic iron oxide MR contrast agents [12, 14] may induce these types of artifacts. Hemochromatosis/iron overload in the liver is increasingly recognized as a possible complication in cancer patients who receive multiple blood transfusions as a part of their therapy [15, 16]. PET quantification errors from tissue misclassification in segmented MRAC images are not only limited to the artifact itself, but can propagate to adjacent tissue [17]. This effect has not been thoroughly investigated before, and to the best of this authors knowledge, no relationship between the distance from an artifact to a potential tumor has been found.

In this thesis, it is argued that the quantification error will show a  $1/d^2$  relationship with the distance ( $d$ ) between a tumor and a misclassified volume. The hypothesis arise from considerations of the well known *inverse square law*. As one of the fields which obey the inverse square law, a point radiation source can be characterized by it. It states that the intensity of radiation is inversely proportional to the square of the distance from the source. However, as the inverse square law applies to point sources, it will be interesting to see if the hypothesis holds for extended sources.

From a phantom study conducted by this author [18], it was found that the error in tumor uptake was proportional to the volume ( $V$ ) of misclassified tissue. It was also argued that the number of *common* line of responses (LORs) of a tumor



and an artifact decides how large the quantification error becomes. In advance, it is believed that the number of common LORs can be directly related to the inverse square law. The results of this thesis show that it may be possible to obtain a linear equation describing the error on a tumor adjacent to the artifact using the ratio  $V/d^2$ . However, we will see that no simple generalization can be made on the task of quantifying these errors, as additional information from the adjacent tissue has to be taken into account. Here, it is suggested that this additional information limits to the activity and attenuation along the common LORs of a tumor and an artifact. This is due to the nature of data collection of PET-systems and also the process used for attenuation correction. The primary aim of this thesis is to study PET uptake errors on tumors adjacent to the susceptibility artifacts, focusing on misclassification of liver tissue (soft tissue) as lung tissue.

Several studies have been conducted attempting to quantify the errors due to artifacts in the attenuation maps. Often, these studies are based on the insertion of simulated artifacts in the PET/MRI data collected from several patients [17, 19, 20]. Taking into consideration the common LOR information, a problem then arises in evaluation of the errors because of inter- (and also intra-) patient variability in attenuation and activity distribution. Therefore, for this thesis data from only a single patient is collected, and both simulated tumors and artifacts are inserted into this patient's PET/MRI data to study the errors. In the aforementioned phantom study [18], no relationship regarding distances could be investigated due to the fixed dimensions of the phantom. For this thesis, a digital phantom is programmed. The relative error (*RE*) in tumor activity is computed from reconstructions of what is assumed to be ground truth PET images from both the digital phantom and the patient, for attenuation maps with and without artifacts, using the ordered subsets expectation maximization (OSEM) reconstruction algorithm. This solution allows to keep both the attenuation and activity along the common LORs similar, while other parameters such as artifact size, tumor size and the distance between these can be varied. We thus manage to limit the influencing factors in a controlled manner.

Because the liver is the largest internal organ in the body [21], it is believed that misclassification of liver tissue has the potential to cause significant underestimation in PET quantification on adjacent tissue, which in the worst case can leave tumors undetected after visual inspection of the images. The results revealed that relevant errors can be introduced to adjacent tumors, even if only parts of the liver are misclassified. Therefore, it is important to come up with correction methods for these types of artifacts. Several strategies for susceptibility artifact correction have been proposed [22]. These include ultra-short echo time (UTE) MRI sequences [12], inpainting methods [23], atlas based methods and more advanced methods such as combination of atlas insertion and

pattern recognition [24]. These methods all have their weaknesses, including time consumption due to manual steps, the need of special software and large patient atlas databases. Here, a solution that can be made fully automatic is devised. It is based on Otsu's method for thresholding, and utilizes the already acquired Dixon data to correct the misclassified liver voxels.

In the next chapter (2), all theoretical concepts relevant for this thesis will be covered. Chapter 3 provides a detailed description of the materials and method used in this thesis. In chapter 4 the results are presented, and are further discussed in chapter 5. Finally, chapter 6 states the conclusions from the thesis.

# /2

## Theory

This section will present basic theory behind the physics and working principles of MRI-, PET- and combined PET/MRI-systems. It will also explain the most important theory behind the image processing and statistical analysis utilized in this thesis.

### 2.1 Basic MRI

A description of the minimum needed, basic theory, on MRI covering the concepts relevant to this thesis will be given in this subsection. The theory leads up to the explanation of how attenuation maps used for AC in hybrid PET/MRI can be derived from magnetic resonance (MR)-data. It will also explain why susceptibility artifacts may occur. Unless stated otherwise, the source of information is from the textbook "MRI from picture to proton" [9].

#### 2.1.1 Physics of MRI

##### Resonance

MRI is derived from nuclear magnetic resonance (NMR). In particular, it exploits the properties of the nuclei of hydrogen atoms as it is abundant in the

human body, especially in water and fat molecules. The nucleus of the hydrogen atom is simply a proton, which is positively charged. All fundamental particles have an inherent quantum mechanical property called spin, which makes them act as they are rotating around their own axis. Basic electromagnetics tells us that a moving charge (i.e. a current) has an associated magnetic field, so the proton generates its own tiny magnetic field known as its magnetic dipole moment,  $\vec{\mu}$ .

If the proton is placed in an external magnetic field it will experience a turning force, known as a torque. This is similar to what happens to a compass needle placed in the Earth's magnetic field. As the compass needle, the proton will try to align itself with the external field, but is constrained by the laws of quantum mechanics. Since the proton cannot align exactly, it continues to experience a torque and starts to precess around the direction of the external field. The well-known analogy for this is the wobbling behavior of a slightly tilted spinning top (gyroscope). A gyroscope will also experience a torque due to the gravitational force and start to precess around the gravitational field lines. The phenomenon is illustrated in figure 2.1.

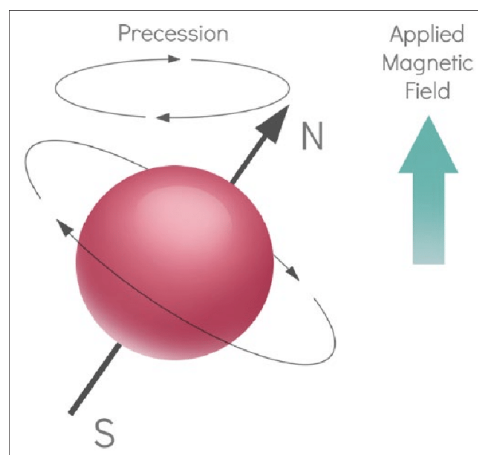


**Figure 2.1:** Illustration of a proton's precession due to an external magnetic field [25].

The precession frequency, also known as the Larmor precession frequency,  $\omega_0$ , of protons is proportional to the external magnetic field and is given by the Larmor equation:

$$\omega_0 = \gamma B_0, \quad (2.1)$$

where  $\gamma$  is a constant named the *gyromagnetic ratio* and is equal to  $2.7 \times$

$10^8 \text{rads}^{-1} \text{T}^{-1}$ . The protons in a magnetic field all precess at the Larmor frequency. This is known as the resonance condition.

## Quantum mechanics

Proton spin is an important part of understanding the origin of an MR signal. At the presence of an external magnetic field, the spin of protons is said to be quantized and it can precess in one of only two orientations; up, being aligned parallel with the main field, or down, being aligned anti-parallel to the external field. The orientation in which a proton chooses to precess depends on its energy. The spin-down orientation requires more energy than that of the spin-up orientation. The statistical distribution of protons between the two states is given by the Boltzmann distribution:

$$\frac{N_{up}}{N_{down}} = \exp\left(\frac{\gamma\hbar B_0}{k_B T}\right) \approx 1 + \frac{\gamma\hbar B_0}{k_B T}, \quad (2.2)$$

where  $\hbar = h/2\pi$  is Planck's constant,  $k_B$  is Boltzmann's constant and  $T$  is temperature. From equation (2.2) we find that the lower-energy state is slightly favored, so that we end up with a net magnetization  $\vec{M}_0$  in the direction aligned *with* the external field, which conventionally is shown as the  $z$ -direction.

## Measuring the magnetic moment

While  $\vec{M}_0$  is parallel to  $\vec{B}_0$  it is virtually impossible to measure it as  $\vec{M}_0$  typically is in the order of micro tesla ( $\mu T$ ) while a typical value for  $\vec{B}_0$  is  $1.5T$  or  $3T$ . To be able to measure  $\vec{M}_0$ , it needs to be tipped into the  $xy$ -plane, the plane transverse to the  $z$ -direction. This is done by applying a radiofrequency (RF) pulse to the precessing protons for a period of time,  $t$ . The RF pulse, created by alternating currents in coils, is perpendicular to  $\vec{B}_0$  and, due to the resonance condition, must be oscillating at the Larmor frequency  $\omega_0$ . In the rotating frame of reference, i.e. from the precessing proton's point of view, this is a static magnetic field  $\vec{B}_1$  in the transverse plane. The flip angle  $\alpha$  of  $\vec{M}_0$  is given by:

$$\alpha = \gamma B_1 t. \quad (2.3)$$

The RF pulse is called a  $90^\circ$  pulse if  $\vec{M}_0$  ends up exactly in the  $xy$ -plane. This process of flipping the magnetization is called excitation. Another important

property of the RF pulse is that it makes the protons precess in phase about  $\vec{B}_0$ , which creates a net magnetization component in the transverse plane  $M_{\perp}$ . This net magnetization produces the measured EM-signal due to the voltage it induces in a receiver coil that only is sensitive to magnetization perpendicular to  $\vec{B}_0$ . The signal is known as the free induction decay (FID). In MRI, the FID is commonly not measured directly, instead echoes are created.

Figure 2.2 shows a schematic representation of the basic principles of MRI we have covered so far. Protons are represented as red balls spinning around their own axis. When  $\vec{B}_0$  (orange arrow) is applied, the protons will align with the direction of  $\vec{B}_0$  in one of the two possible orientations, spin-up, or spin-down. The difference between the protons aligned parallel and anti-parallel to  $\vec{B}_0$  (blue ball) represents the protons that are responsible for the MRI signal. The sum of these protons can be described by  $\vec{M}_0$  (blue arrow). If a second magnetic field ( $\vec{B}_1$ ) orthogonal to  $\vec{B}_0$  is applied, it is possible to tilt  $\vec{M}_0$  of  $90^\circ$  along the  $xy$ -direction ( $M_{\perp}$ , green arrow). When  $\vec{B}_1$  is switched off,  $\vec{M}_{\perp}$  returns to the equilibrium through two *relaxation* processes.

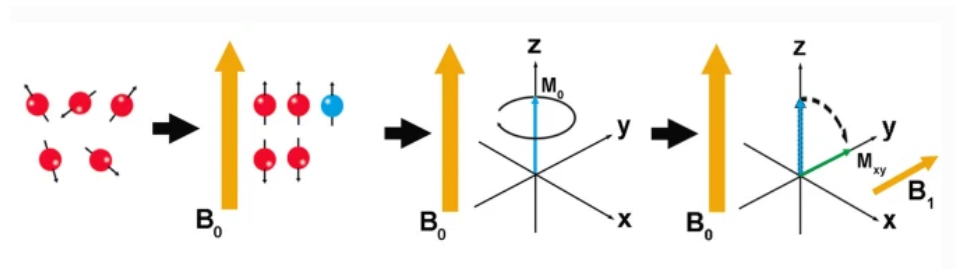


**Figure 2.2:** Schematic representation of the basic principles of MRI [26].

## Relaxation

Generally, there are two relaxation processes towards an equilibrium: (1) spin-lattice relaxation and (2) spin-spin relaxation.

(1): Due to the torque of the external magnetic field, the magnetization vector  $\vec{M}_0$  will begin to realign with  $\vec{B}_0$  immediately after the RF pulse is switched off. The process where the protons begin to relax their way from the higher energy, excited state to their equilibrium position is known as  $T_1$  spin-lattice relaxation. To lose energy, the protons interact with surrounding tissue and, as this happens, the protons gradually return to their spin up/spin down states and eventually become aligned with  $\vec{B}_0$ . A schematic representation of this process is given in figure 2.3.

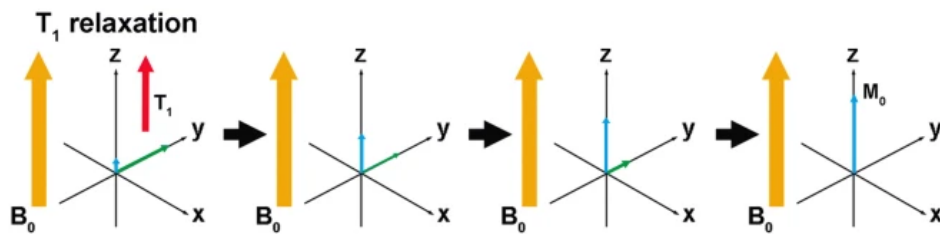


Figure 2.3: Schematic representation of  $T_1$  relaxation [26].

(2): Spin-spin relaxation comes from the dephasing of the spins following their phase coherence after the RF pulse. Although this makes the transverse magnetization decay, there are no net loss of energy in this form of relaxation. A schematic representation of this process is given in figure 2.4.

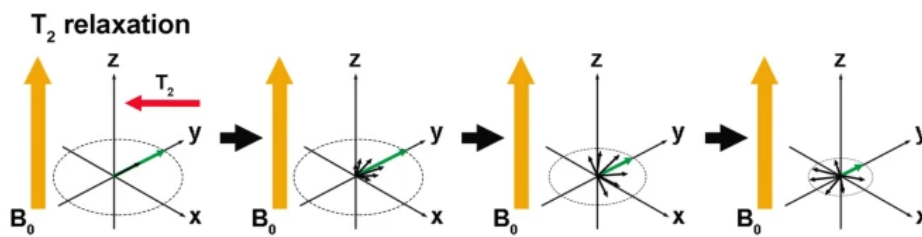


Figure 2.4: Schematic representation of  $T_2$  relaxation [26].

In the former process (1), i.e. the spin-lattice  $T_1$  *longitudinal* relaxation,  $T_1$  is defined as the time it takes for the  $z$ -component of the net magnetization to reach  $1 - \frac{1}{e} \approx 63\%$  of its original size. The latter process (2), the relaxation in the  $xy$ -plane, or the spin-spin  $T_2$  *transverse* relaxation, is dominated by the unavoidable inhomogeneity in  $\vec{B}_0$ , but also the spin-spin interactions.  $T_2$  defines the time it takes for the  $xy$ -component of magnetization to fall to  $\frac{1}{e} \approx 37\%$  of its original size following the RF pulse. Unlike  $T_1$ , which increases with field strength,  $T_2$  is independent of field strength, and in human tissues,  $T_2$  is always shorter than  $T_1$ .

## Spatial encoding

To be able to localize the origin of a radiated RF signal, spatial encoding is required in MRI. This is done by using gradients to record the two- (or three-) dimensional spectrum of the object being measured. This spectrum is known as *k-space* and is a matrix of individual spatial frequencies.

The gradient coils create an additional spatially linear variation in  $\vec{B}_0$  and can be applied in any direction or orientation. An MRI system typically has three sets of gradient coils,  $G_x, G_y, G_z$ , which give MR its three-dimensional capability. Mathematically, the three orthogonal gradients of  $\vec{B}_0$  are defined as:

$$G_x = \frac{\partial \vec{B}_0}{\partial x}, G_y = \frac{\partial \vec{B}_0}{\partial y}, G_z = \frac{\partial \vec{B}_0}{\partial z}. \quad (2.4)$$

When a gradient is applied, the total field experienced by nuclei will be dependent upon the position in space. This also alters the Larmor precession frequency of nuclei so that it too becomes spatially dependent. For example, the  $z$ -gradient will be affected as follows:

$$\omega = \gamma(B_0 + zG_z). \quad (2.5)$$

This spatial encoding, performed in the  $z$ -direction, is better known as *slice selection* and the  $G_z$  gradient is often referred to as the slice selection gradient,  $G_{SS}$ . The same can be done for the  $x$ - and  $y$ -directions, also referred to as the frequency- and phase-encoding directions, respectively.

### 2.1.2 Contrast in MRI

In general, images in MRI have contrast which depends on either  $T_1, T_2$  or proton density (PD) and can be *weighted* towards any of these by adjusting two operational parameters: echo time (TE) and repetition time (TR). TE is the time interval from excitation to the maxima of the following echo, and TR is the time interval between excitations.

TE and TR are easiest to get an understanding of by discussing the spin echo (SE) sequence. It involves a  $90^\circ$  excitation pulse, meaning the magnetization vector  $M_0$  is flipped all the way into the transverse plane, repeated every TR. At time  $TE/2$  following the  $90^\circ$  RF pulse, a  $180^\circ$  pulse is applied. This rephases the protons that are dephased due to inhomogeneities in the magnetic field, creating an echo at time TE which is recorded. A mathematical description of MR signals was given by Bloch in 1946 [27], where a set of equations used to calculate the magnetization in the transverse plane  $M_\perp$  were proposed. The Bloch equation also clearly shows the effect of TE and TR on the MRI signal



when solved for the SE sequence:

$$M_{\perp}(TR, TE) = M_0(1 - e^{-\frac{TR}{T_1}})e^{-\frac{TE}{T_2}}. \quad (2.6)$$

From (2.6), we see that at a relatively long TR ( $TR \gg T_1$ ), the effects of  $T_1$  largely disappear as the factor  $(1 - e^{-\frac{TR}{T_1}}) \rightarrow 1$ . For short TE ( $TE \ll T_2$ ), the same is true for  $T_2$  as  $e^{-\frac{TE}{T_2}} \rightarrow 1$ .

To get a  $T_1$  weighted image, short TR and TE are required, while long TR and TE are required to get a  $T_2$  weighted image. PD weighted images are obtained from short TE and long TR, whereas the opposite configuration gives too small signals to be useful.

Another common MRI sequence is the gradient echo (GE) sequence. In these sequences, the echoes recorded are created by gradient coils, meaning the dephasing due to field inhomogeneities is not reversed. Instead of  $T_2$ , the observed signal will now be dependent on a composite relaxation time  $T_2^*$  which includes  $T_2$ , inhomogeneities due to differences in the main field and tissue susceptibility, and diffusion of the protons. Unlike SE, GE sequences often utilize flip angles ( $\alpha$ ) smaller than  $90^\circ$  which results in the following equation for the transverse magnetisation:

$$M_{\perp}(TR, TE, \alpha) = M_0 \frac{(1 - e^{-\frac{TR}{T_1}})e^{-\frac{TE}{T_2^*}}}{1 - \cos(\alpha) \cdot e^{-TR/T_1}}. \quad (2.7)$$

The same observations as in equation (2.6) can be made here. Equation (2.7) explains why iron accumulation in the liver may cause signal loss in GE MRI sequences. The magnetic properties of iron induces a faster spin dephasing and thus a shorter  $T_2^*$ . This means the factor  $e^{-\frac{TE}{T_2^*}} \rightarrow 0$ , and we get signal loss.

### Tissue contrast and magnetic susceptibility

A natural property of all tissues is their magnetic susceptibility  $\chi$ . It is a measure of how magnetized the tissue becomes when placed in a strong magnetic field and depends on the electron arrangement in the tissue. In general, there are four types of magnetic susceptibilities. *Diamagnetic* materials show very weak magnetic susceptibility and as they produce an internal field in the opposite direction of the external field. In the human body, most tissues are diamagnetic,

while air and dense bone have  $\chi \approx 0$ . *Paramagnetic* materials show stronger susceptibility and tends to align with the external field, producing a field in the same direction. Paramagnetic materials in the human body are e.g. deoxy-haemoglobin and met-haemoglobin. *Superparamagnetic* materials are those intermediate between paramagnetic and ferromagnetic, and examples include iron oxide particles, which are common in MR contrast agents. *Ferromagnetic* materials experience a large force when placed in an external field as they easily become strongly magnetized. Metal alloys containing iron are often ferromagnetic. Although the magnetic susceptibility of tissues is small, the differences between e.g. tissues and air are large enough to induce local magnetic field gradients. This means that hydrogen atoms on either side of the boundary will experience different magnetic fields and will interact with each other and relax more quickly.

The susceptibility problems may degrade the *homogeneity* of the external magnetic field. The homogeneity of a magnet describes the uniformity (or the quality) of its field, and reduced homogeneity can result in image degradation and artifacts. As explained previously in this section, GE images should be called  $T_2^*$  weighted, and not  $T_2$  weighted. This is because of the effects of magnetic field inhomogeneities due to an imperfect magnet or susceptibility effects in the patient. Air pockets, dense bone and iron-rich blood breakdown products (met-haemoglobin) present in the human body all affect the main magnetic field in their immediate vicinity. These inhomogeneities further affect the relaxation of tissues after being excited by an RF pulse, speeding up the apparent spin-spin relaxation  $T_2^*$ . GE images depend on these spin-spin relaxation times  $T_2^*$ . The GE sequences are thus more sensitive to magnetic field inhomogeneities than SE sequences.

### 2.1.3 Dixon method

As described in subsection 2.1.1, protons precess at the Larmor frequency when placed in a magnetic field. However, this frequency is not the same for all hydrogen protons because it has a dependency on the shielding effects of the molecule's electron shell [28]. As a result, water and fat molecules have slightly different resonance frequencies and go in- and out-of-phase with each other as a function of time. This is known as a *chemical shift*, and the period of this phase cycling is directly proportional to the magnetic field strength. In-phase and opposed-phase conditions occur twice per cycle, as illustrated in figure 2.5. The figure illustrates the phase cycling at a magnetic field strength of 1.5T, where it appears approximately every 2.2 msec. At 3.0T, it is twice as fast, occurring every 1.1 msec [28].

The type of chemical shift, known as type 2 chemical shift, which is the subject

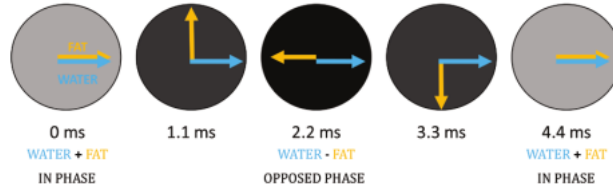


**Figure 2.5:** Figure shows that fat and water protons precess at different frequencies. Their phases completely cancel at TE of 2.2 msec (opposed-phase), and are additive at TE of 4.4 msec (in phase) [28].

of this thesis, occurs only with GE-imaging [28]. As mentioned before, GE-sequences lack the  $180^\circ$  rephasing pulse that SE-sequences offer. Signal loss due to susceptibility thus manifests with a signal intensity loss on the in-phase images, because the longer TE allows for more  $T_2^*$  decay to occur.

In 1984, Thomas Dixon suggested a method for creating images of just fat and water [9, p. 93]. The solution eventually became to combine the in-phase and opposed-phase GE images, with the idea that the signal in the in-phase image  $S_{ip}$  is the sum of the signals from fat  $S_f$  and water  $S_w$ :

$$S_{ip} = S_w + S_f. \quad (2.8)$$

The signal in the opposed-phase image  $S_{opp}$  is the difference:

$$S_{opp} = S_w - S_f. \quad (2.9)$$

By simple addition, subtraction and averaging, water-only and fat-only images can be found:

$$\frac{1}{2}(S_{ip} + S_{opp}) = \frac{1}{2}(S_w + S_f + S_w - S_f) = S_w \quad (2.10)$$

$$\frac{1}{2}(S_{ip} - S_{opp}) = \frac{1}{2}(S_w + S_f - S_w + S_f) = S_f. \quad (2.11)$$

This is the fundamental theory behind how attenuation maps are derived from MRI. The post-processing steps in order to derive attenuation maps from the Dixon data will be explained later (section 2.3.1).

## 2.2 Basic PET

In this subsection, the basic theory on the physics and working principles of PET scanners are presented. Particularly important is the part on the mathematics of attenuation correction, which is the fundamental theory behind the methodology chosen in this thesis, i.e. it explains how simulated tomography experiments can be conducted. Unless stated otherwise, the source of information is from the textbook "PET: Physics, Instrumentation, and Scanners" [29].

### 2.2.1 Physics of PET

#### Positron emission

An atomic nucleus consists of nucleons (protons and neutrons). Inside a nucleus, two opposing forces are acting: The *strong force*, which is an attractive force between nucleons, and the repulsive *coulomb force* between the positively charged protons. An unstable nucleus has either an excess number of protons or neutrons, which creates an unbalance in the opposing forces and makes the nucleus prone to radioactive decay. A radioactive decay leads to a change in the number of protons or neutrons in the nucleus and a more stable configuration. Such decay prone nuclei are known as radionuclides. PET is a nuclear imaging technique that exploits the unique decay characteristics of radionuclides that decay by positron emission ( $\beta^+$ -decay or beta-plus-decay). The process of beta-plus-decay is essentially the conversion of a proton into a neutron, positron ( $e^+$ ) and neutrino( $\nu$ ). An example of a radionuclide that decays in such a manner is  $^{18}\text{F}$ :



The net released energy during positron emission is shared between the resultants; the daughter nucleus, the positron and the neutrino.

#### Annihilation

A positron ejected following a  $\beta^+$ -decay has a very short lifetime in tissue due to the high electron density of tissue. Its kinetic energy rapidly decreases as inelastic interactions with atomic electrons ( $e^-$ ) in the tissue occur. Once it has lost most of its energy it will combine with an electron, its anti-particle, and the masses of both particles will be converted into photons. This process is known as *annihilation*. Because the electron and positron are almost at rest when

this occurs, the energy released comes largely from the mass of the particles. The energy can be computed from Einstein's famous mass-energy equivalence as:

$$E = mc^2 = m_{e^-}c^2 + m_{e^+}c^2, \quad (2.13)$$

where  $m_{e^-}$  and  $m_{e^+}$  are the masses of the electron and positron, respectively, and  $c$  is the speed of light. Inserting values into equation (2.13), we find that  $E = 1.022$  MeV. This energy is released in the form of two high energy photons, and because the particles are almost at rest when the annihilation occurs, the net momentum is close to 0. From the laws of conservation, we know that both energy and momentum must be conserved, as would *not* be the case if only one photon was emitted. Then, we would get a net momentum in the direction of the photon. Instead, we get two photons that are simultaneously emitted  $180^\circ$  apart, i.e. in opposite directions. As the particles not necessarily are perfectly at rest at the time of annihilation, the direction of the emitted photons is not exactly  $180^\circ$ , but very close to. For energy to be conserved, it must be evenly distributed between the two photons so each photon will have an energy of  $511keV$ . These high energetic photons belongs to the gamma portion of the electromagnetic spectrum, and have a good chance of escaping the body for external detection. This lead directly to the fundamental concept of PET. Thus, a PET scanner is designed to detect and localize simultaneous annihilation photons emitted following a  $\beta^+$ -decay.

### Photon interactions in matter

The two dominant mechanisms by which  $511keV$  photons interact with matter in the human body are through photoelectric effect and Compton scattering. The former describes the process when the energy of a photon is completely absorbed by an atomic orbital electron (generally inner shell). This causes the electron to escape the atom with an energy equal to that of the incident photon, and the energy of the electron is rapidly absorbed by the surrounding tissue. An outer-shell electron then fills the vacancy and causes an x-ray with energy equal to the binding energy of the electron to be emitted. In Compton scattering, the incident photon transfers part of its energy to an outer shell, essentially a "free" electron ejecting it from the atom. The photon, which has excess energy, is scattered at an angle depending on the amount of energy it has lost due to ejecting the electron [30].

## Linear attenuation coefficient

Interactions, including both absorption and scattering of annihilation photons in matter, can be described by the exponential relationship:

$$I(x) = I_0 \exp(-\mu x), \quad (2.14)$$

where  $I_0$  is the initial photon intensity,  $x$  is the thickness of matter which a photon traverses, and  $\mu$  is the linear attenuation coefficient (LAC).  $\mu$  describes the probability per unit distance that an interaction will occur.

In the case of 511 keV photons, it is largely described by the influence of photoelectric absorption and Compton scattering:

$$\mu \approx \mu_{photoelectric} + \mu_{Compton}. \quad (2.15)$$

Table 2.1 shows linear attenuation coefficients for some tissue types that are of interest in this thesis.

**Table 2.1:** Linear attenuation coefficients for different tissue types [8, p. 56].

Tissue class	Linear attenuation coefficient ( $\mu$ )
Air	$0.0\text{cm}^{-1}$
Lung	$0.0224\text{cm}^{-1}$
Fat	$0.0854\text{cm}^{-1}$
Soft tissue	$0.1000\text{cm}^{-1}$

### 2.2.2 PET image formation

#### Photon detection

PET cameras must have a high efficiency for detecting 511 keV photons. *Scintillation* detectors are widely used gamma-ray detectors that form the basis for almost all PET scanners today. A typical PET-system consists of a large number of detectors placed around the object to be imaged, and the most common detector configuration is the ring geometry. With a ring geometry, the PET scanners FOV is the space enclosed by the detector ring.

Scintillation is a form of luminescence that applies specifically to the light emission from crystals exposed to photons from radiation. The process of

converting photon energy to light can be summarized as absorption of the photon energy by the crystal, leaving it in an excited state. The gamma photon transfers its energy in photoelectric and Compton interactions. As the excited electrons in the crystal return to their original state, they release photons in the visible portion of the electromagnetic spectrum. In most standard clinical PET scanners, photo-multiplier tubes (PMTs) are used to convert these photons into electrical signals, but unfortunately, PMTs are very sensitive to external magnetic fields [31]. Hybrid PET/MRI systems therefore use the semiconductor analog of PMTs, called avalanche photodiodes (APDs), and these magnetically insensitive semiconductor photodiodes are capable of operating in high magnetic fields. In addition, APDs are also more compact, have a higher quantum efficiency and require a lower supply voltage than PMTs.

### Coincidence detection

In PET collimators are not required. Instead, PET cameras are based on the detection of simultaneous and oppositely directed 511 keV photons. This is referred to as *coincidence detection*. The absence of collimators results in a high sensitivity of the detectors. If two detectors located on opposite sides of the annihilation register coincident photon impacts, we know that the annihilation occurred along a line between these detectors. This line is referred to as a LOR. A coincidence circuit makes sure mostly true coincidence events are counted, that is, events that arise from a single annihilation. Unfortunately, the true coincidences registered are contaminated with undesirable events, which include *random*, *scattered* and *multiple* coincidences due to interactions within the patient. These events have a degrading effect on the final image and need to be corrected to produce an image that gives a best possible representation of the radioactive distribution within the FOV [30]. Figure 2.6 illustrates the four main coincidence event types.

To improve the overall detection efficiency, the detectors of modern PET systems usually extend 15 cm or more in the axial direction. This can be accomplished by stacking several rings of detectors next to each other. Many slices of data can then be acquired simultaneously, ultimately producing a set of image slices that can be stacked into a 3-D image volume. The detectors are designed to record as many of the annihilation photons as possible. Therefore, in block detector systems, each detector is in electronic coincidence with a fan of detectors on the opposite side of the ring. This is illustrated in figure 2.7, where we can observe that the object is simultaneously sampled from many different angles.

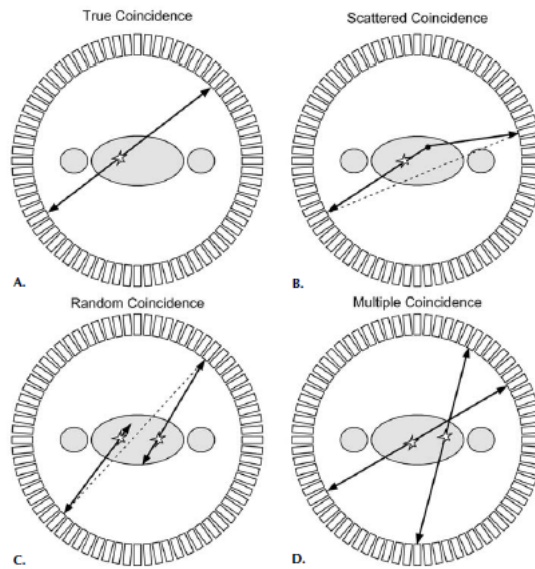


**Figure 2.6:** Illustration of the four main coincidence event types [29, p. 36].

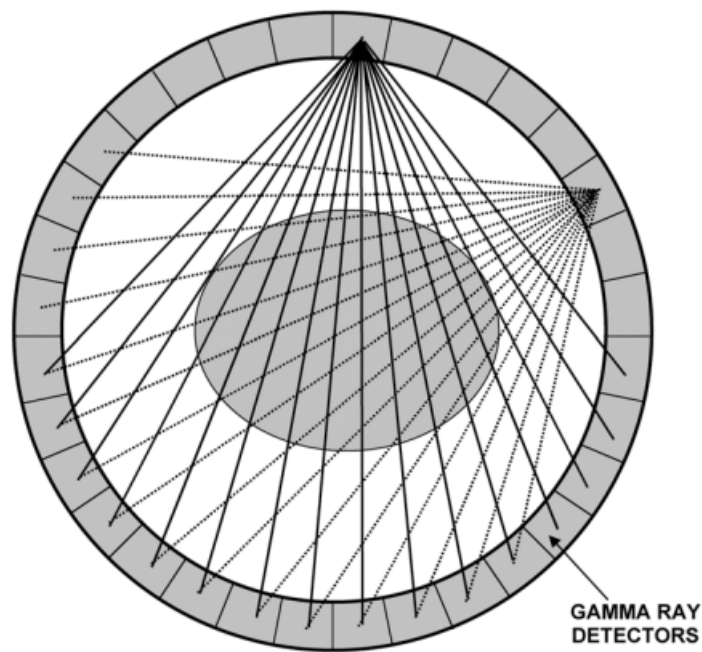


**Figure 2.7:** Schematic drawing of a PET scanner of ring geometry. [29, p. 8].



## Time of flight

As a sidebar, theory on time of flight (TOF) is included here. It is not considered elsewhere in this thesis, because it is not a feature of the PET/MRI machine the patient dataset were collected from.

As described above, coincidence detection only localizes the annihilation photons to within a line joining the detector pairs. To get a more precise measurement as to where on this line the annihilation occurred, TOF-information can be used. This method involves computing the difference in arrival time,  $\Delta t$ , of the two photons at the detectors, and the location  $d$  of the annihilation with respect to the half-way point between the two detectors:

$$d = \frac{\Delta t \times c}{2}, \quad (2.16)$$

where  $c$  is the speed of light. In practice, with the currently available detector technology, the positional resolution with TOF information is in the order of  $cm$ , instead of the desired accuracy of a few  $mm$ . As stated by Cherry, "even a timing resolution as fine as 100 ps would only yield a positional resolution of  $\approx 1.5$  cm" [29, p. 8].

## Data representation - the sinogram

The raw data acquired by a PET-scanner consists of the detection of annihilation photon pairs. It is usually histogrammed into a 2D matrix, where each matrix element corresponds to the number of events recorded by a specific pair of detectors, i.e. along a LOR. Each row of the matrix consists of data acquired at a different angle of rotation  $\phi$  from  $0^\circ$  to  $180^\circ$ , i.e. projections of the activity at a particular  $\phi$ . Each column represents the radial offset  $r$  from the center of the scanner. Which element in the  $r, \phi$  matrix that relates to the radioactivity at location  $(x, y)$  is given by the relationship:

$$r = x \cos(\phi) + y \sin(\phi) \quad (2.17)$$

A point source at a location  $(x, y)$  traces a sinusoidal path in the matrix  $s(r, \phi)$ , which is known as a sinogram. Figure 2.8 illustrates the formation of the sinogram based on a 12 detector PET system. In such a 2D mode, there is a separate sinogram for each slice location along the axial direction of the patient.

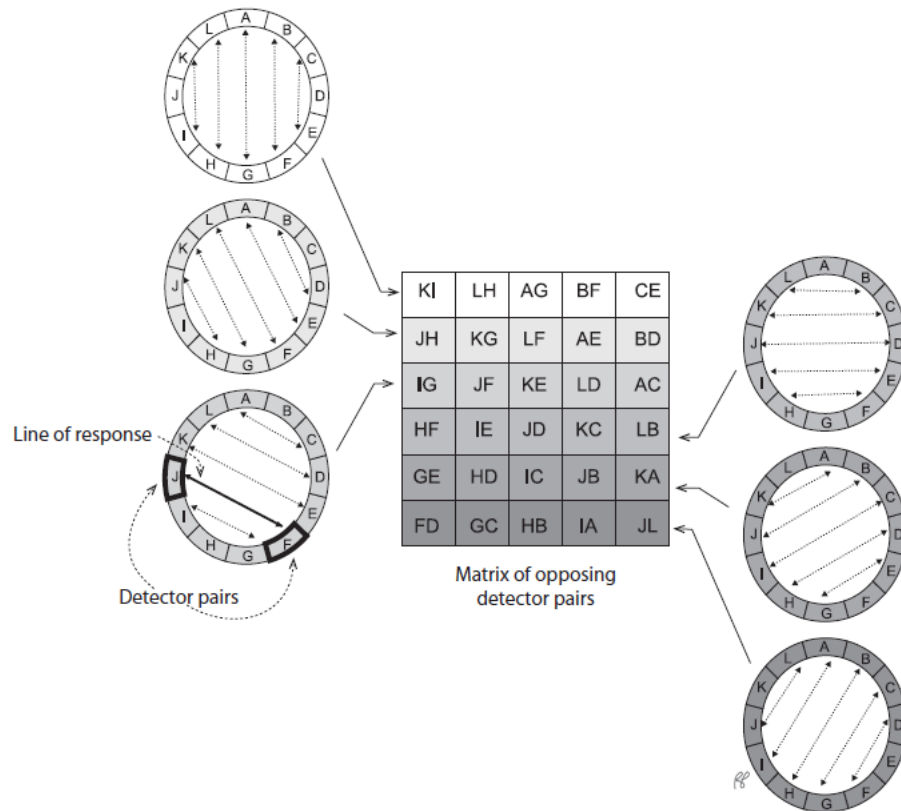


Figure 2.8: Illustration of the formation of a sinogram [30, p. 179].

### 2.2.3 Image reconstruction

As the PET raw data only defines the location of the pairs of annihilation photons in the object being scanned to within a LOR across the object, image reconstruction is necessary. The role of the reconstruction step is to convert the LORs into a 2D or 3D image that quantitatively reflects the distribution of positron-emitting atoms within the object. There are two basic approaches to image reconstruction. One is analytic in nature and utilizes the mathematics of computed tomography to relate the LOR measurements to the activity distribution. Common algorithms that does this include filtered back projection and Fourier reconstruction [29]. A second approach is to use iterative methods that, in a series of successive iterations, attempt to model the data collection process and find the image that is most consistent with the measured data.

In this thesis, reconstructions are done with the iterative OSEM algorithm, which is an accelerated version of the popular maximum likelihood expectation maximization (MLEM) algorithm. The OSEM algorithm has become

a major workhorse in today's scanners [29]. Maximum likelihood (ML) is a standard statistical estimation method which essentially assumes a statistical model for the measured data, and expectation maximization (EM) is an efficient algorithm to find the ML estimate. While reconstruction quality of the MLEM algorithm is good, the application of EM is slow and computer intensive. Within each iteration, the OSEM algorithm processes the data in subsets and thus accelerates convergence with a factor proportional to the number of subsets.

A full description of the implementation of OSEM is beyond the scope of this thesis. All relevant information on the algorithm can be found in the original published paper [32].

#### 2.2.4 Attenuation correction

The probability of 511 keV photons interacting with matter in the human body before hitting the detectors is relatively high. The result of this is the potential detection of scattered photons in a different LOR, or attenuation or removal of primary photons from a given LOR. To be able to provide accurate quantification of the radioactive distribution, it is thus necessary to correct for photon attenuation in the reconstruction process. This process is known as AC.

AC accounts for the fact that annihilation photons originating from deeper locations within the object must pass through more matter, and therefore has a higher probability of being attenuated on its way to the detector. Figure 2.9 shows the effect of AC for a cylinder with uniform radioactivity distribution, where it can clearly be observed that the outer edges of the cylinder appear to have a higher activity than the central portion. This demonstrates the need for AC to obtain quantitatively accurate representations of the radioactive distribution within the patient.

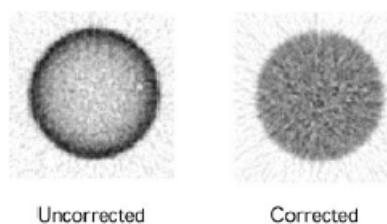


**Figure 2.9:** Effect of AC on a cylinder with uniform activity distribution [29, p. 57]

The matter enclosed by the detector's FOV includes scanner hardware components, e.g. table top, RF coils, positioning aids, etc., and patient tissues,

which all need to be considered in the AC as they potentially can attenuate photons.

### 2.2.5 The mathematics of attenuation correction

In computed tomography, the reconstruction problem is to obtain a tomographic slice image from a set of projections. The projections are formed by drawing a set of parallel rays through the 2-D object of interest for different angles between the rays with respect to the object. The collection of all projections at several angles creates the previously described sinogram and the implementation of this is known as the *Radon transform*, which can be used to simulate a tomography experiment. The interested reader is referred to [33] for a wealth of information on the Radon transform.

To get a grasp on the problem of attenuation correction in PET we consider the idealized, two-dimensional example as given by Berker and Li [34], following their exact notation. Their problem formulation goes as follows: Consider two positive, real functions representing spatial distributions of radioactivity concentrations ( $\lambda$ , activity map) and linear attenuation coefficients ( $\mu$ , attenuation map) where we wish to create a mapping  $\lambda, \mu: \mathbb{R}^2 \rightarrow \mathbb{R}_0^+$ , where  $\mathbb{R}_0^+$  denotes the set of non negative real numbers.  $\lambda, \mu$  are assumed sufficiently smooth and decaying towards 0 rapidly enough such that all following integral expressions are well-defined. Lines in the plane are parameterized by polar coordinates,  $(s, \phi) \in [\mathbb{R} \times [0, 2\pi)]$ . The distance to  $(0, 0)$  is given by  $s$ , and the angle with the  $y$ -axis is given by  $\phi$ . With  $l$  a parameter along the line, we thus have, in vector notation:

$$\mathbf{x}_{s,\phi}(l) = s\hat{\mathbf{u}} + l\hat{\mathbf{n}}, \quad (2.18)$$

where  $\hat{\mathbf{u}} = (\cos(\phi), \sin(\phi))^T$  and  $\hat{\mathbf{n}} = (-\sin(\phi), \cos(\phi))^T$  are unit vectors. Figure 2.10 illustrates a line  $L$  indicated by its parameterization  $(s, \phi)$  and the  $(s, l)$  coordinate system, rotated by  $\phi$  with respect to  $(x, y)$ .

Further, Berker and Li [34] states that in PET, we can describe measurements without attenuation by the non-attenuated *activity sinogram*,  $p$ , where  $p: \mathbb{R} \times [0, 2\pi) \rightarrow \mathbb{R}_0^+$

$$p(s, \phi) = R(\lambda(s, \phi)) := \int_{-\infty}^{\infty} dl \, x_{s,\phi}(l), \quad (2.19)$$

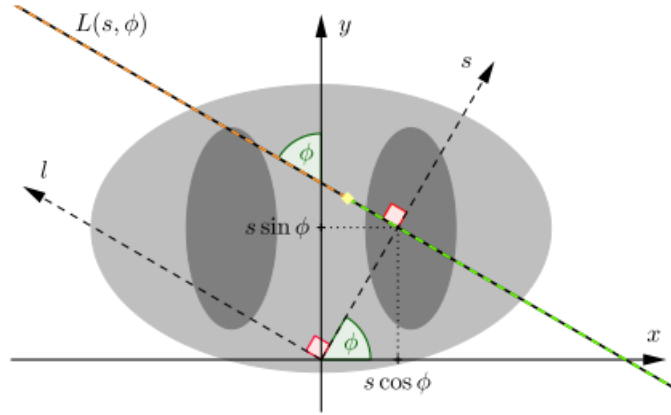


**Figure 2.10:** Illustration of the parameterization to polar coordinates. [34]

where  $R(\cdot)$  denotes the Radon transform.

In PET, the count of detected annihilation photons by each detector corresponds to the measurement of the concentration of radiotracer along some part of the line on which the detector lies. This amounts to knowing the value of the Radon transform along a portion of that line [33, p. 35]. Since the photons travel through some attenuating material, they lose energy. Because of this, Berker and Li [34] calls the need of the attenuated activity sinogram,  $m$ , which describes the measured data:

$$m(s, \phi) = \int_{-\infty}^{\infty} dl \, x_{s, \phi}(l) \cdot a(s, \phi, l). \quad (2.20)$$

Here,  $a(s, \phi, l) : \mathbb{R} \times [0, 2\pi) \rightarrow (0, 1]$  denotes the *attenuation factors*. The attenuation factors are independent of the position along the line  $l$ . With help of the Beer-Lambert law, the relation of  $a$  to the attenuation map is given as:

$$a(s, l, \phi) = a(s, \phi) = \exp\left[-\int_{-\infty}^{\infty} dr \mu(x_{s, \phi}(r))\right]. \quad (2.21)$$

The fact the attenuation factors is independent of the position along the line means that attenuation effects are constant along each LOR. Hence,  $a$  can therefore be separated from the integrand, from which it follows that (2.20) simply is the Radon transform of  $\lambda$  multiplied with  $a$ , which in turn is given by

the Radon transform of the attenuation map:

$$m = a \cdot R(\lambda) = \exp[-R(\mu)] \cdot R(\lambda). \quad (2.22)$$

This theory is the basis for the simulated tomography experiments conducted in this thesis. Assuming that we have a ground truth PET image ( $\lambda^*$ ), or activity map as Berker and Li [34] named it, and an attenuation map ( $\mu$ ) available, the data that are uncorrected for attenuation can be estimated. This is what Berker and Li referred to as the *attenuated activity sinogram*, which describes the measured data of the PET system.

To perform AC, hybrid imaging modalities such as combined PET and CT (PET/CT) and PET/MRI creates an estimate  $\hat{\mu} \neq \mu$  of the attenuation map by the CT/MRI part of the system. For hybrid PET/CT systems, AC is obtained by performing a low dose (80 – 140keV) CT scan of the patient. This latter approach is a transmission measurement, where the CT part acts as an external radiation source. Because the photon-tissue interactions occurring in PET and CT build on the same physical principles, the data obtained from the CT scan can be converted to LACs at the 511 keV photon energy levels used for PET. This usually provides a quite accurate geometric representation of the tissue distribution as Hounsfield units (HU) [2]. The PET/MRI hybrid system cannot measure LACs as the MR part does not give any information about the electron density of the tissue, i.e. there are no one-to-one relationship between the MR signal and the photon attenuation in tissue. Instead, MRI commonly use AC maps based on a Dixon sequence to create an estimate of the distribution of attenuating elements in the FOV. This approach is known as segmentation based MRAC, and the idea behind it is to partition the image into a given set of tissue classes and assign a pre-defined attenuation coefficient to the tissue class each image voxel belongs to. The number of tissue classes varies between PET/MRI manufacturers. The attenuation corrected image  $\lambda$  can thus be obtained according to equation 2.24:

$$\lambda = R^{-1}(a^{-1} \cdot m) = R^{-1}(\exp[R(\hat{\mu})] \cdot m) \quad (2.23)$$

$$= R^{-1}(\exp[R(\hat{\mu})] \cdot \exp[-R(\mu)] \cdot R(\lambda)). \quad (2.24)$$

### 2.3 Hybrid PET/MRI systems

Hybrid PET/MRI systems combine the physiological and molecular imaging capability of PET with the excellent anatomical imaging capability of MRI. Unlike

PET/CT machines, PET/MRIs not only provides reduced ionizing radiation and improved soft tissue contrast, but also a range of MR specific variations such as functional MR, spectroscopic NMR and diffusion tensor imaging. The fusion of the two image modalities has proven to be very challenging due to the mutual detrimental effect on each other's performance. The technical challenges and design solutions of PET/MRI systems are beyond the scope of this thesis, but more information on the issue can be found in [35]. Figure 2.11 shows the system design of a hybrid PET/MRI scanner.

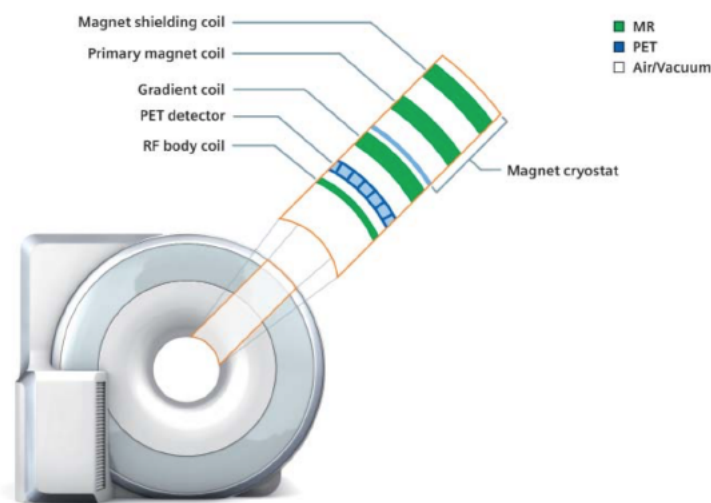


**Figure 2.11:** Illustration of a hybrid PET/MRI system [2, p. 244]

### 2.3.1 MRAC on the Siemens Biograph mMR

The following description of AC on the Siemens Biograph mMR, from which patient image data is collected from in this thesis, is adopted from Catana [7] where a description of the attenuation correction methods applied by the main vendors of clinical PET/MRI-machines are given:

In the approach adopted for the Siemens Biograph mMR scanner (Siemens Healthineers, Erlangen, Germany) the whole body is segmented into four tissue classes (air, lung, fat and soft tissue) from the MR data collected using a two-point Dixon volume interpolated breath-hold exam (VIBE) sequence. Only the data from the thorax is acquired at breath hold, and in-phase, out-of-phase, water and fat images are generated at each bed position. By applying threshold operations to the fat and water images, voxels corresponding to fat and soft tissue are obtained. Lung tissue is identified as regions of low signal, and

the lungs are segmented by connected component analysis of the internal air cavities. A morphological closing filter is applied to minimize misclassification of bone, heart and aorta as air. The respective LACs for the different tissue types are given in table 2.1. Ultimately, a 3-D Gaussian filter is applied to generate the attenuation map that is combined with the hardware attenuation map during reconstruction. [7]

From this, it becomes clear that in the presence of susceptibility artifacts, regions of lowered signals in the MR-data may cause the threshold operations to fail, and tissue misclassification occurs. When this occurs in tissue around the lungs, e.g. in the liver, the connected component analysis may falsely identifies these low intensity regions as lung tissue.

## 2.4 Image processing

This section describes the basic theory behind the image processing steps conducted in chapter 3. Unless stated otherwise, the source of information is the textbook "Digital Image Processing" [36]. The notation is, for the most part, identical to the cited source.

### 2.4.1 Image segmentation

#### Thresholding

Due to its simple and intuitive properties, thresholding has a central position in applications of image segmentation. In its simplest form, the method chooses pixels in an image  $f(x, y)$  with an intensity greater than or less than some fixed threshold constant  $T$ . In this way, a segmented image  $g(x, y)$  can be created:

$$g(x, y) = \begin{cases} 1 & f(x, y) > T \\ 0 & f(x, y) \leq T. \end{cases} \quad (2.25)$$

Often thresholding problems are more difficult, involving a histogram with several dominant modes corresponding to different objects. If we consider a case with two lighter objects on a dark background, multiple thresholding can classify a pixel as belonging to the background if  $f(x, y) \leq T_1$ , to one object class if  $T_1 < f(x, y) \leq T_2$ , and to the last object class if  $f(x, y) > T_2$ . That is,



the segmented image is given by:

$$g(x, y) = \begin{cases} a & f(x, y) > T_2 \\ b & T_1 < f(x, y) \leq T_2 \\ c & f(x, y) \leq T_1, \end{cases} \quad (2.26)$$

where  $a, b, c$  are three distinct label values. Figure 2.12 illustrates histograms for which the described methods, i.e. single thresholding and multiple thresholding, may be applied.

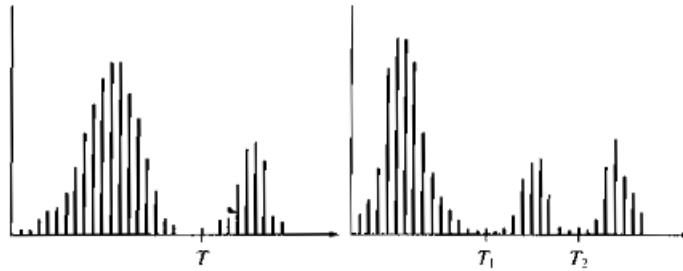


**Figure 2.12:** Illustration of intensity histograms that can be partitioned by (left) single threshold and (right) multiple thresholds. [36, p. 743]

### Otsu's method

In the view of statistical-decision theory, thresholding may be viewed as a problem whose objective is to minimize the average error from assigning pixels to two or more groups or *classes*. The Bayes decision function is an elegant and well known closed-form solution to this problem. Otsu's method is an attractive alternative to this, as it avoids the process of estimating any probability density functions and can be implemented for real-time applications. Otsu's method is optimal in the sense that it maximizes the between-class variance, or equivalently, minimizes the intra-class variance between two (or more) classes. It is thus a one-dimensional discrete analog of Fisher's Discriminant Analysis, and equivalent to a globally optimal k-means [37]. In addition to its optimality, an important property of Otsu's method is that it is solely based on computations performed on the histogram of an image, which is easily obtained as a 1-dimensional array. The following description of the implementation of Otsu's method adopted from Gonzalez [36]:

Assume an image of size  $M \times N$  is represented in  $L$  intensity levels,  $\{0, 1, 2, \dots, L-1\}$ . Let the number of pixels at intensity level  $i$  be denoted by  $n_i$ , and the total

number of pixels in the image be  $MN = n_0 + n_1 + \dots + n_{L-1}$ . The probability of intensity level  $i$ ,  $p_i = n_i/MN$ , from which it follows that:

$$\sum_{i=0}^{L-1} p_i = 1, \quad p_i \geq 0. \quad (2.27)$$

For the two class case, a threshold,  $T(k)$  is selected such that the pixels of the image are divided into two classes,  $C_1, C_2$ , with intensity levels  $[0, k], [k + 1, L - 1]$ , respectively.

Using the threshold, the respective probability distributions for the two classes  $C_1, C_2$  are:

$$P_1(k) = \sum_{i=0}^k p_i \quad (2.28)$$

$$P_2(k) = \sum_{i=k+1}^{L-1} p_i = 1 - P_1(k). \quad (2.29)$$

The respective means of classes  $C_1, C_2$  are:

$$m_1(k) = \frac{1}{P_1(k)} \sum_{i=0}^k ip_i \quad (2.30)$$

$$m_2(k) = \frac{1}{P_2(k)} \sum_{i=k+1}^{L-1} ip_i \quad (2.31)$$

and the global mean of intensity levels,  $m_G = P_1 m_1 + P_2 m_2$ .

The effectiveness of the threshold at level  $k$  can be evaluated by the normalized dimensionless measure:

$$\eta(k) = \frac{\sigma_B^2(k)}{\sigma_G^2}, \quad (2.32)$$

where  $\sigma_G^2$  is the global variance, given by:

$$\sigma_G^2 = \sum_{i=0}^{L-1} (i - m_G)^2 p_i, \quad (2.33)$$

and  $\sigma_B^2(k)$  is the between-class variance, given by:

$$\sigma_B^2 = P_1(k)(m_1(k) - m_G)^2 + P_2(k)(m_2(k) - m_G)^2. \quad (2.34)$$

The optimal threshold is the value of  $k$  that maximizes equation (2.32), and thus maximizes the between-class variance [36].

### Region growing

As the name implies, region growing is a region-based segmentation method that groups pixels into regions based on predefined criteria for growth. Commonly, we start with a set of "seed" points from which regions are grown by appending to each seed those neighboring pixels that have similar properties to the seed. The similarity measure can be e.g. ranges of intensity or color. The formulation of a stopping rule is just as important as the criteria for growth when it comes to performance of region growing algorithms. The growth should stop when no more pixels satisfy the criteria for inclusion in that region, but criteria such as intensity values, color and texture only consider local conditions and do not take into account the "history" of the growth. The performance of region growing algorithms can be greatly improved by additional criteria that utilize the concepts of size, region statistics or shape, but these types of descriptors are based on the assumption that an *a priori* model of expected results is (partially) available. [36]

## 2.5 Statistical analysis

This section explains the relevant theory for the statistical analysis utilized in this thesis. The source of information is the textbook "Introduction to Statistics and Data Analysis" [38].

### 2.5.1 Linear regression

Regression analysis is in many fields one of the most widely used techniques of quantitative research. In any area of research where one is interested in studying the relationship between a variable of interest, called the response variable, and a set of explanatory variables, regression analysis can be utilized.

In *linear* regression models, one aims to find a linear relationship between the response variable,  $y$ , and the explanatory variable  $x$  from a set of observations  $(x_i, y_i)$ . Thus, a linear function is created:  $y = ax + b$ . Here,  $b$  represents the intercept of the line with the  $y$ -axis, and  $a$  represents the slope of the line. However, as each observation potentially deviates by  $e_i$  from the line given by the function, the linear model can be written as follows to take this into account:  $y_i = ax_i + b + e_i$ . Each deviation  $e_i$  is called an error, and represents the deviation of the observations from the regression line.

Suppose we are given a data set of  $n$  observations  $(x_i, y_i)$ . By the *method of least squares*, one can determine  $a$  and  $b$  such that the sum of the squared distances between the observations and the line  $y = ax + b$  is minimized. We thus fit a line to the data set such that the errors are minimized:

$$\min_{a,b} \sum_{i=1}^n e_i^2 = \min_{a,b} \sum_{i=1}^n (y_i - ax_i - b)^2. \quad (2.35)$$

This is an optimization problem that can be solved by the principle of minima to obtain the estimates of  $a$  and  $b$ , denoted  $\hat{a}$  and  $\hat{b}$  respectively.

By comparing an observation  $(x_i, y_i)$  with the point predicted by the regression line  $(x_i, \hat{y}_i)$ , their difference is called the *residual*, and is given by:  $\hat{e}_i = y_i - \hat{y}_i = y_i - (\hat{a}x_i + \hat{b})$ . The residuals are not the  $e_i$ s themselves, but an estimate.

A quantitative measure of the "goodness" of fit for a regression model is given by the  $R^2$  value. This value indicates how much variation of a response variable is explained by the explanatory variable(s). It can be derived by variance decomposition of the data, where the total variation of  $y$  is partitioned into two components: sum of squares due to the fitted model and sum of squares due to random errors in the data, from which we get the formula:

$$R^2 = 1 - \frac{\text{Unexplained variation}}{\text{Total variation}} \quad (2.36)$$

From this, it follows that  $0 \leq R^2 \leq 1$ , and the closer  $R^2$  is to 1, the better the fit. An  $R^2$  of 1 means that all variation in the response variable is completely explained by movements in the explanatory variable(s).

The residual standard error, also known as the root mean squared error (RMSE), is also a useful measure of describing the fit of a model. It is defined as the square root of the variance of the residuals, i.e. the standard deviation of the residuals. The RMSE is an absolute measure of fit, in contrast to  $R^2$  which is a relative measure of fit. It also has the useful property of being in the same units as the response variable, and tells how wrong the regression model is on average. A small RMSE value indicates a better fit, because it means observations are closer to the fitted line.



# /3

## Materials and methods

In this chapter, the steps taken in order to study the effect of susceptibility artifacts on adjacent tumors is presented in detail (section 3.1). The focus is on susceptibility artifacts leading to the false assignment of lung tissue attenuation values to liver tissue. A method for correcting voxels in the attenuation map that has been falsely assigned the attenuation value of lung tissue is also proposed (section 3.2).

### 3.1 Artifact impact on adjacent tumors

Observer interest in the segmented MRAC images is not in the display of images, but instead in their application to AC. In the quantitative evaluation of errors in such images, we need to look at how the errors show up in the reconstructed PET images. The method chosen in this thesis is inspired by the work of Hofmann et al. [24]. In their study, differences in reconstructed 2-D PET-image slices were compared for attenuation maps from a CT transmission scan to those from predicted pseudo-CT images. Here, 2-D PET image slices are reconstructed, but for attenuation maps with and without simulated susceptibility artifacts. Simulated PET avid tumors at varying distances from the artifact are inserted into, what is assumed to be, ground truth PET images. To assess the errors, the relative change in activity of the simulated tumors is calculated from the PET images reconstructed with attenuation maps with and without artifacts.

Below follows a description of how emission data and attenuation maps were acquired, allowing to run simulated tomography experiments from 2-D image slices of a digital phantom and realistic patient dataset. After that, descriptions of how the digital phantom was created and how simulated tumors and artifacts were inserted into the patient dataset are given. All relevant Python code that was implemented can be found in the appendix (A.2).

### 3.1.1 Acquiring emission data and attenuation maps for reconstruction

As a starting point for the study, 2-D ground truth PET images ( $\lambda^*$ ) and attenuation maps ( $\mu$ ) are assumed available. In order to study how errors in attenuation maps with artifacts ( $\mu_{art}$ ) propagated to the reconstructed PET image ( $\lambda$ ), the attenuated activity sinogram ( $m$ ) had to be obtained from  $\lambda^*$  and  $\mu$ . This was done according to formula (2.22), i.e.:

$$m = \exp[-R(\mu)] \cdot R(\lambda^*).$$

In this way, emission data similar to the form that the PET-scanner measures it was obtained. It would be better if raw sinogram data could be obtained directly from the PET/MRI-machine, but this dataset could not be accessed due to problems with handling the (binary) format of these files. The Radon transform was implemented using the *transform* module of the *scikit-image* [39] Python library. The number of projections was chosen to be 256 between angles  $0^\circ$  to  $180^\circ$ , equivalent to having 256 detector pairs. The Siemens Biograph mMR consists of a PET detector with 8 rings and 56 detector blocks in each ring. This yields a total of 224 detector pairs in the axial FOV of 25.8 cm [40] that potentially can measure a coincidence from an image slice within the axial FOV of the scanner. As the Radon transform is a computationally heavy operation, a large number of projection angles would cause the simulated tomography experiment to run slowly. Therefore, the number of projection angles were chosen based on a trade-off between time and resolution.

In attenuation maps, LACs are typically given in units  $\text{cm}^{-1}$ , or some scaled version of this. Therefore, these had to be converted to unit  $\text{pixel}^{-1}$  to be valid for reconstruction. From the spatial pixel spacing of the images, of unit  $[\text{mm}/\text{pixel}]$ , a simple conversion factor (CF) was obtained:

$$\text{CF} [\text{cm}/\text{pixel}] = \frac{\text{pixel spacing} [\text{mm}/\text{pixel}]}{10 [\text{mm}/\text{cm}]} \quad (3.1)$$



The attenuation maps were multiplied with the conversion factor prior to performing the Radon transform.

Because the reconstruction method is not perfect,  $m$  was reconstructed with both  $\mu$  and  $\mu_{art}$  to neglect any errors introduced by the reconstruction algorithm. The respective reconstructed PET images  $\lambda$ ,  $\lambda_{art}$  were obtained as:

$$\lambda = \text{Rec}(m \cdot \exp[\text{R}(\mu)]) \quad (3.2)$$

$$= \text{Rec}(\exp[-\text{R}(\mu)] \cdot \text{R}(\lambda^*) \cdot \exp[\text{R}(\mu)]) \quad (3.3)$$

$$= \text{Rec}(\text{R}(\lambda^*) \cdot \exp[\text{R}(\mu) - \text{R}(\mu)]) \quad (3.4)$$

$$= \text{Rec}(\text{R}(\lambda^*)) \quad (3.5)$$

and

$$\lambda_{art} = \text{Rec}(m \cdot \exp[\text{R}(\mu_{art})]) \quad (3.6)$$

$$= \text{Rec}(\exp[-\text{R}(\mu)] \cdot \text{R}(\lambda^*) \cdot \exp[\text{R}(\mu_{art})]) \quad (3.7)$$

$$= \text{Rec}(\text{R}(\lambda^*) \cdot \exp[\text{R}(\mu_{art}) - \text{R}(\mu)]). \quad (3.8)$$

$\text{Rec}(\cdot)$  denotes the reconstruction method which in this thesis was implemented using the OSEM algorithm from the Tomopy library in Python [41]. Differences in  $\lambda_{art}$  and  $\lambda$  are dependent on the exact used reconstruction method. However, the focus in this thesis was not to compare different reconstruction methods. For the simulated PET images, 2-D slices were reconstructed with OSEM, neglecting normalization, scatter and random coincidences to isolate the bias on activity due to artifacts in the attenuation maps only. The hyperparameters of the OSEM algorithm, i.e. the number of iterations ( $NI$ ) and number of subsets ( $NS$ ), were chosen by searching for the combination of  $NI$ ,  $NS$  that gave the reconstructed image most similar to the ground truth image when reconstructed with the attenuation map without artifacts:

$$\min_{NI, NS} |\lambda - \lambda^*|. \quad (3.9)$$

It was found that  $NI = 12$  and  $NS = 1$  gave the best result.

As the change in activity of a simulated tumor was of interest, the tumor was for each reconstruction defined as a volume of interest (VOI), and the mean

relative error (RE) was calculated according to equation (3.10):

$$RE[\%] = \frac{\text{mean}[\lambda_{art}^{VOI}] - \text{mean}[\lambda^{VOI}]}{\text{mean}[\lambda^{VOI}]} \cdot 100\%, \quad (3.10)$$

where  $\lambda_{art}^{VOI}, \lambda^{VOI}$  denotes the VOI, being the tumor, on the PET-images reconstructed with  $\mu$  and  $\mu_{art}$ , respectively.

### 3.1.2 Creation of a digital phantom

Phantom experiments are widely used in the field of medical imaging to evaluate and analyze the performance of imaging modalities. To the best of this author's knowledge, a PET/MRI phantom where one can insert, and vary the placement of, volumes of high activity does not exist. Performing measurements on physical phantoms can also be a time consuming task which exposes the persons performing the experiment to unnecessary amounts of ionizing radiation. Instead of making an attempt of building such a phantom, for this thesis, a digital phantom was programmed using Python 3.9. The digital phantom was designed to operate in 3-D, but only the 2-D slice of maximal radii of the simulated tumors and artifacts was chosen for reconstruction due to limited computational resources. This means the artifact and tumor volumes are given in 2-D area. Figure 3.1 shows a 2-D slice of the digital phantom. A description of how the digital phantom was created follows below.

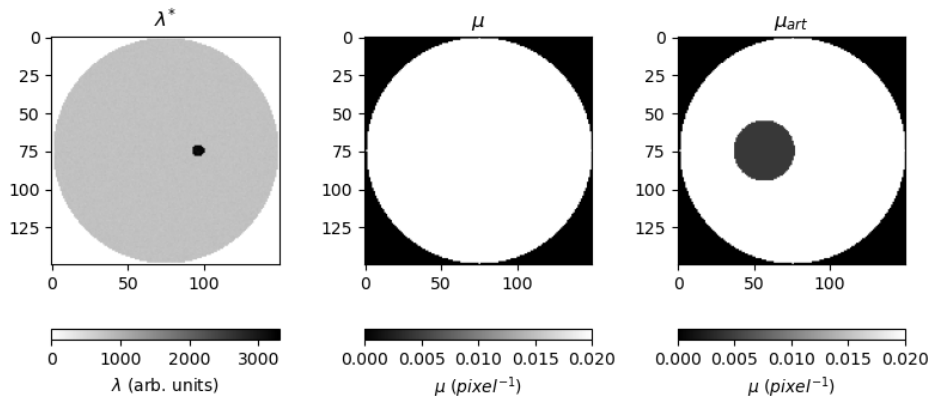


**Figure 3.1:** Illustration of 2-D slice for  $\lambda^*$ ,  $\mu$  and  $\mu_{art}$  for the digital phantom. TBR = 4.

For reconstructions, ground truth activity maps ( $\lambda^*$ ) and attenuation maps ( $\mu, \mu_{art}$ ) were needed. These were created as separate 3-D image volumes of

dimensions  $150 \times 150 \times 150$ . As the digital phantom was designed to mimic a sphere of water-like soft tissue, spheres containing the information on activity and attenuation were inserted into the image volumes. These were of diameter 148, which left one row/column in the edges of the 3-D image volumes empty. This was a requirement for the Radon transform algorithm.

Because positron emission itself is well characterized by the Poisson distribution [42, 43, 44], the spherical volume in  $\lambda^*$  was filled with background activity values drawn from a Poisson distribution. Smaller, spherical high activity regions, mimicking PET avid tumors, could then be placed at any location within the image volume (figure 3.1). For  $\mu$  and  $\mu_{art}$ , the attenuation value of soft tissue was assigned to all voxels within the spherical volume. For voxels outside, the attenuation values were set to 0, representing air. To simulate artifacts in  $\mu_{art}$ , smaller, spherical volumes was inserted where the attenuation value of lung tissue replaced that of soft tissue. The phantom was created with an isotropic voxel spacing of  $2 \times 2 \times 2$  mm/voxel, yielding a physical diameter of 29.6 cm to the overall phantom. A conversion factor as described in equation (3.1) was calculated and multiplied with the attenuation maps to obtain the correct attenuation value for each voxel.

### 3.1.3 Setups of the digital phantom

Individual reconstructions were run for several different setups of the digital phantom, where tumor diameter, artifact diameter and the distance between the center points of the tumor and artifact was varied. The range tumor diameters were 1.0, 1.2, 1.6, 2.0 cm, all relevant tumor sizes for primary tumor characteristics according to the TNM cancer grading system [45]. To obtain more statistics and to investigate the effect of tumor activity on the quantification error in the presence of artifacts, several tumor-to-background ratios (TBRs) were investigated. The TBRs were selected to 1.5, 2, 4, 8. The artifact diameters were selected to 1.0, 2.0, 4.0, 8.0, 12.0 cm. 12 cm was chosen as the maximal artifact diameter, because it is comparable to the mean liver size of men, at 10.5 cm [46]. A liver span up to 2 cm larger is also considered normal [46]. The tumor distances to the artifacts was in the range of 1.2 to 21 cm between their center points. As the interest was on how errors propagated outside the artifact, all cases where a tumor and artifact overlapped were removed. The cases where any point in a tumor exceeded the dimensions of the image were also removed. Reconstructions were done for all combinations of TBRs, tumor diameters and artifact diameters for all valid distances. The purpose of the digital phantom experiment was not to obtain any realistic quantification, but to see how the different factors influenced the error on adjacent tumors.

In figure 3.1, the phantom setup for tumor diameter of 1.6 cm, artifact diameter

of 8 cm and a distance of 8 cm between their center points is illustrated for TBR equal to 4. The setup in figure 3.1 was used for studying the effect of tumor activity on the error. To evaluate this effect, contour plots of the relative error in the whole reconstructed images were created:

$$\text{Relative error contour plot} = \frac{\lambda_{art} - \lambda}{\lambda}. \quad (3.11)$$

To validate the assumption that the quantification error of an adjacent tumor depends on the information on common LORs with the artifact, a noise-free phantom reconstruction was also run. The setup for the reconstruction can be seen in figure 3.2.

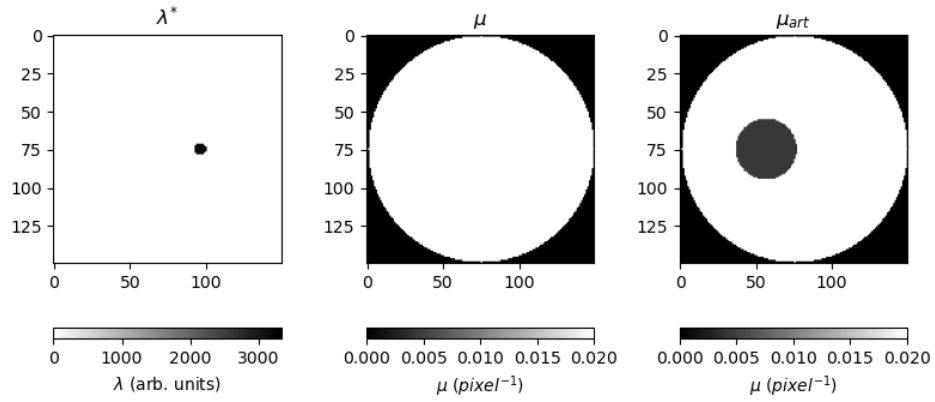
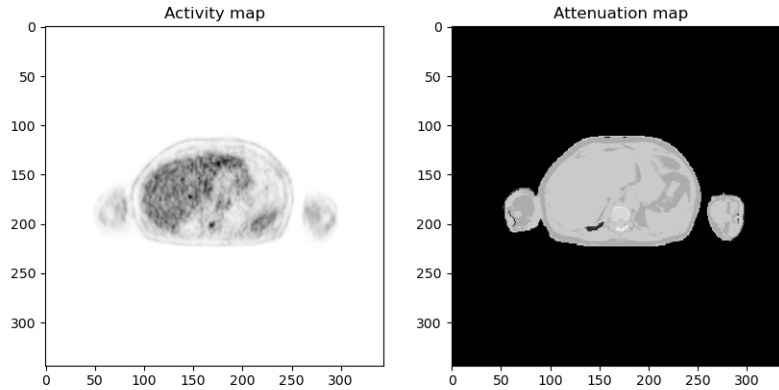


Figure 3.2: Noise free phantom setup.

### 3.1.4 Simulating tumors and artifacts in a patient dataset

To see if the discoveries made in the digital phantom experiment could be transferred to a realistic situation, a dataset from a patient who underwent a whole body  $^{18}\text{F}$ -FDG PET/MRI examination on the Siemens Biograph mMR PET/MRI-machine at the University Hospital of Northern Norway (UNN) was collected (appendix A.1). Because misclassification of liver tissue as lung tissue occurs when the MR signal from liver tissue is too low to be distinguished from the nearby lung tissue, a 2-D axial slice where both the liver and lung were visible was selected for analysis. The original activity map and attenuation map of the selected slice is seen in fig 3.3.

The size of the axial PET image slice was  $344 \times 344$ , with a pixel spacing of  $2.08262 \times 2.08262$  mm/pixel. The size of the axial image slice of the attenuation



**Figure 3.3:** Figure of the activity map (left) and attenuation map (right) of the selected slice from patient for analysis.

map was  $287 \times 412$ , with a similar pixel spacing as that of the PET image. To be able to reconstruct the PET image with the attenuation map, these had to be of similar sizes. Therefore the attenuation map was registered and resampled to match the PET image, i.e.  $344 \times 344$ . This was done using the *Resample image* module in *3D Slicer* [47, 48]. To avoid introducing any new information in the resampled attenuation map, the interpolation method was chosen to be nearest neighbor. The resampled image slice of the reference attenuation map ( $\mu$ ) is shown to the right in figure 3.3.

To create  $\mu_{art}$ , circular artifacts of different diameters with lung-equivalent density were inserted into  $\mu$ . This was done manually with use of the *pyplot.ginput* function of the *matplotlib* [49] Python library. The artifact diameters used were 1.0, 2.1, 4.2, 8.3 cm. Larger artifact diameters than these were not included because we wanted the artifacts to be contained within the liver. From the Dicom metadata of the patient PET images, it was found that the PET-images had been smoothed with a Gaussian filter of 3 mm full width at half maximum (FWHM). Therefore, after multiplying with the conversion factor as described in equation 3.1, the attenuation maps were also convolved with a 3 mm FWHM Gaussian kernel prior to reconstruction. This was done with the *filters* module of the *skimage* Python library. To create the ground truth PET-images ( $\lambda^*$ ), simulated tumors of 1.67 cm was placed on the PET image slice in fig 3.3. Each tumor was placed within the patients liver, as this was a region that showed homogeneous uptake. Again, this was done with use of the *pyplot.ginput* function of the *matplotlib* [49] Python library. This allowed to run individual simulated tomography experiments and reconstruct PET-images with tumors at different distances from an artifact (section 3.1).

With the assumption that the information, i.e. activity and attenuation, along common LORs of a tumor and an artifact was crucial for the magnitude of the quantification error, two situations were considered. In the first, for each artifact size, a tumor was placed at 10 different distances along a line from the artifact. Individual reconstructions were run for each tumor-artifact distance. For each reconstruction, the tumor thus had similar information along its common LORs with the artifact. Figures 3.4 and 3.5 show the tumor's locations (blue points) and the center point of the artifact (orange points) for artifact diameters of 1.0 cm and 8.3 cm, respectively.

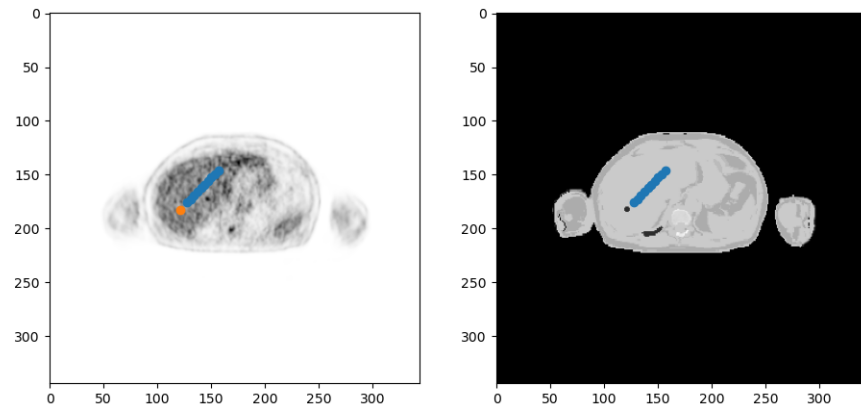


**Figure 3.4:** Illustration of placement of tumors and artifact where the artifact diameter is 1.0 cm. Tumors placed along a line.

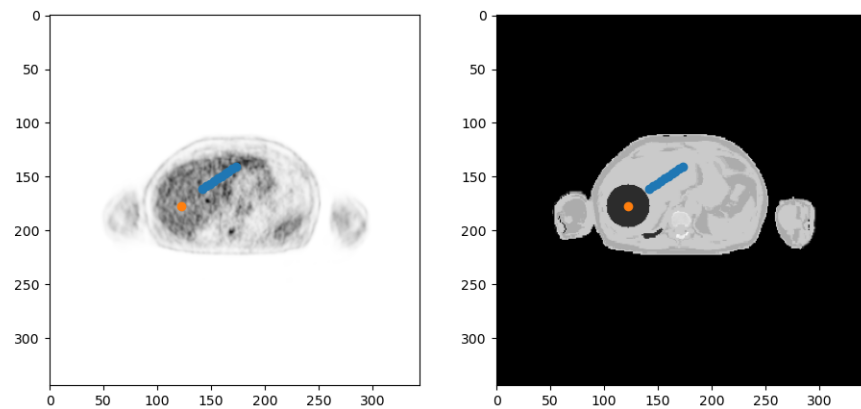


**Figure 3.5:** Illustration of placement of tumors and artifact where the artifact diameter is 8.3 cm.

Next, individual reconstructions were run for the tumor placed at 10 random

locations around the artifact. Thus, for each tumor-artifact distance, the tumors common LOR information with the artifact was randomized. This was done for the same artifact diameters as before, i.e. 1.0, 2.1, 4.2, 8.3 cm. The tumor locations for artifact diameter of 8.3 cm is illustrated in figure 3.6.

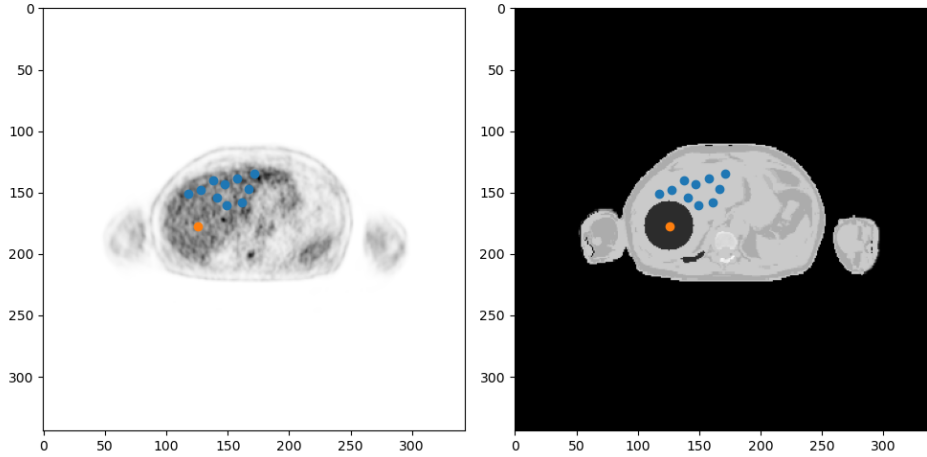


**Figure 3.6:** Illustration of placement of tumors and artifact where tumors have been randomly placed.

Because no patient information was available, e.g. weight, no SUV calculations could be done. Therefore, the TBR was used to decide the activity in the simulated tumors. Kim et al. [50] found that malignant nodules showed a SUV ratio versus liver of  $2.09 \pm 0.96$ . To obtain sufficient statistics, the liver activity of the patient was found by calculating the mean activity in 10 spherical VOIs of 2 cm inside the liver. The average uptake of these were found to be 2042 Bq/ml. The activity of the simulated tumors was therefore set to be 4000 Bq/ml, giving a TBR of 1.96.

As all changes in the attenuation map will lead to changes in the reconstructed image, we also looked at which of our artifact sizes that introduced what can be considered a *relevant difference*. Because the mean activity in VOIs was compared (equation 3.10), a difference was considered relevant if it was larger than the variation in the mean activity in VOIs of the same size in a region of homogeneous activity distribution. To determine this variation, the mean value of the VOIs used for determining the activity of the inserted tumors was calculated:

$$avg = \frac{\sum_{k=1}^{10} VOI_k}{10}. \quad (3.12)$$

The level of significance ( $\Delta_{sig}$ ) was then set to the standard deviation of the means of the VOIs:

$$\Delta_{sig} = \frac{\sqrt{\frac{\sum_{k=1}^{10} (VOI_k - avg)^2}{9}}}{avg} \cdot 100\% \quad (3.13)$$

### 3.2 Correction method for lung-liver misclassifications

In the reported cases [10, 11, 12] where iron overload has shown to cause misclassification of liver tissue as lung tissue, the opposed-phase image from the T1-weighted Dixon MR sequence revealed normal moderate MR signal intensity. The corresponding in-phase image has demonstrated signal loss due to susceptibility artifact from excessive iron accumulation in the liver. This motivated using the opposed-phase image as an "atlas" to correct the wrongly assigned voxels. By doing so, the common problems of atlas/template-based correction methods, such as image registration problems and the need for large patient databases, are effectively eliminated. It also guarantees perfect anatomical match of the data used for correction with the attenuation map itself.

As no realistic patient data where this artifact is present could be obtained from the PET/MRI scanner in Tromsø, it was synthetically introduced into the data from the same patient as used for the previous study. A combination of thresholding and region growing was applied to the Dixon water image to segment the liver, and create a boolean liver mask. The water image was chosen because the liver showed most contrast to the surrounding tissue/organs there. The segmentation was done using the *Segment editor* module of 3D Slicer [47, 48]. A number of seed points for region growing were placed inside the liver, and the growing stopped when it reached background voxels, i.e. voxels outside the liver. The background was found by using global thresholding. Figure 3.7 shows the workspace in 3D Slicer where the liver have been segmented from the Dixon water image.

The full 3-D datasets of the water and opposed-phase Dixon images, in the vertical, horizontal and axial directions, were of sizes  $240 \times 412 \times 157$ , while the attenuation map was of size  $287 \times 412 \times 157$ . Therefore, the water and opposed-phase images were registered to the attenuation map and resampled to obtain similar sizes of the datasets, again using the *Resample Image* module of 3D Slicer [47, 48] with nearest neighbor interpolation. The (3-D) attenuation



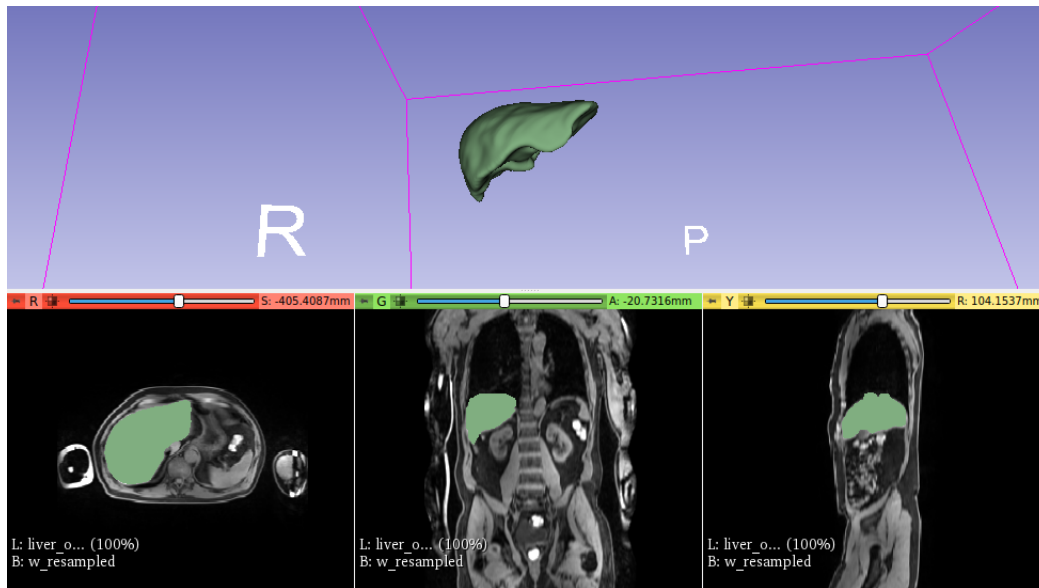


**Figure 3.7:** The workspace in 3D Slicer showing the segmentation of the liver. The top image shows the whole 3D segmentation and the bottom row an axial (left), coronal (middle) and saggital (right) slice.

map, opposed-phase image and liver segmentation mask were exported as Dicom image files from 3D Slicer for further processing in Python, where the correction algorithm was implemented.

### 3.2.1 Correction algorithm

To introduce the artifact where the full liver had been wrongly assigned the attenuation value of lung-tissue, the 3-D boolean liver mask was used to change all values in the attenuation map where the mask had value 1. Figure 3.8 shows a coronal slice of the original attenuation map, and the same slice where the artifact has been introduced.

To correct the image, first, a 3-D correction mask was obtained, i.e. all voxels in the attenuation map that have the attenuation value of lung tissue. Using this correction mask, the corresponding voxels in the 3-D opposed-phase image was extracted. By use of the *skimage* [39] Python library, Otsu's method was applied on the histogram of their intensity values. From this, a threshold to separate soft tissue voxels from lung tissue was obtained. All voxels that were included in the mask, and had a value greater than the obtained threshold, were assigned soft tissue attenuation value in the attenuation map. The implementation of the suggested correction method is given as Python code in the appendix

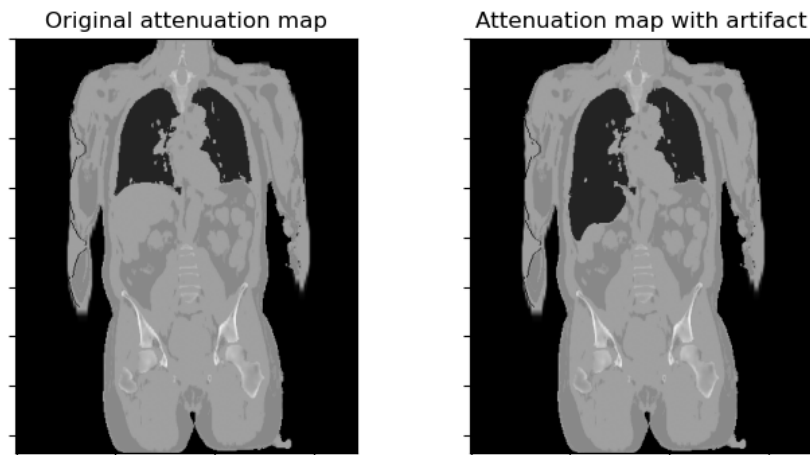


**Figure 3.8:** Coronal slice of original attenuation map (left) and the same slice where the artifact has been introduced (right).

(A.3).

As data from only one patient was available, this dataset was modified in order to test the method for varying liver signal intensities in the opposed-phase image. To achieve this, the liver mask was used to reduce the intensity value of liver voxels in the opposed-phase image. This was done simply by multiplying all voxels in the opposed-phase image, contained in the mask, by a reduction factor  $< 1$ . Figure 3.9 shows examples of a coronal slice with different liver signal intensities.

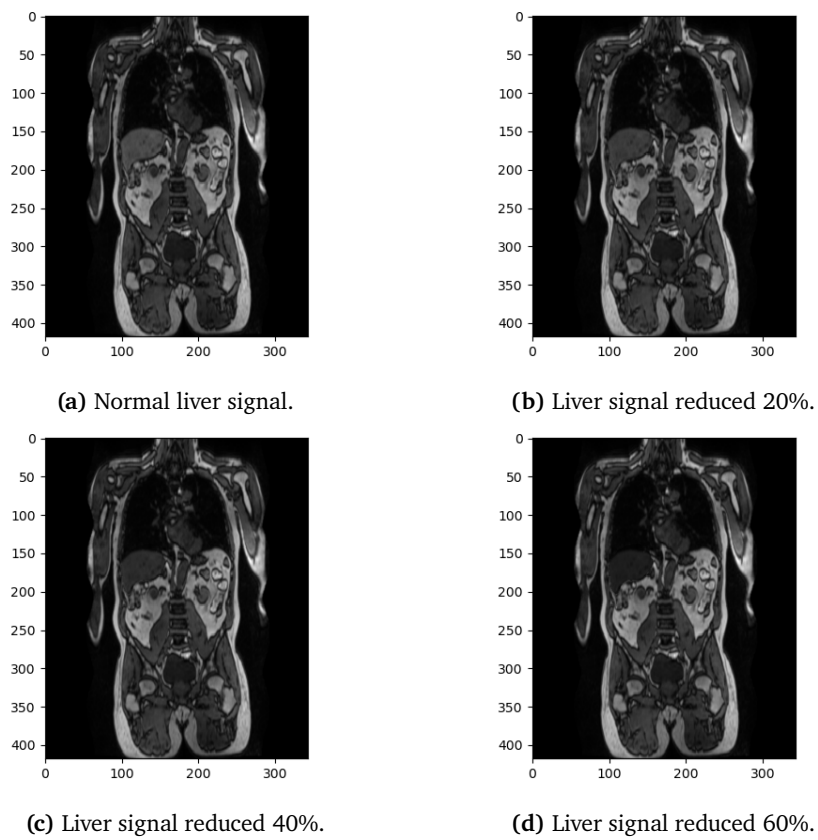


**Figure 3.9:** Illustration of opposed-phased images with different liver signal intensities.



# /4

## Results

This chapter contains the results from the studies described in chapter 3. The chapter is split into two sections; the first, section 4.1, presents the results from the study on misclassifications in segmented MRAC images. The second, section 4.2, shows the performance of the proposed correction method for misclassification of liver tissue as lung tissue.

### 4.1 Artifact impact on adjacent tumors

Here, the results obtained from the experimental method described in section 3.1 are given. First, the findings of the effect of tumor-artifact distance are presented. Thereafter, the effect of tumor activity is illustrated. All linear regression analysis performed to obtain the results has been done with use of the *statsmodels* [51] Python module.

#### 4.1.1 Effect of tumor distance to artifacts in segmented MRAC images

##### Reconstructions on the digital phantom

The purpose of the digital phantom experiment was not to obtain any quantitatively valid results, but rather to investigate the effect of susceptibility artifacts

on adjacent tumors in a controlled manner, such that any observations made in a realistic case could be explained or supported. As explained in section 4.1, several phantom setups were created. Individual reconstructions were performed for each setup, where tumor diameters, artifact diameters, TBRs and the distance ( $d$ ) between the center points of each tumor and artifact was varied. From the reconstructed images,  $\lambda$ ,  $\lambda_{art}$ , the  $RE$  (equation 3.10) of the tumors was calculated. The goal of this was to observe any dependency of the  $RE$  on  $d$ . The  $RE$  was expected to have a linear dependency on the volume of an artifact ( $V$ ) [18]. Therefore, in each plot, data points are grouped with respect to the artifact diameters.

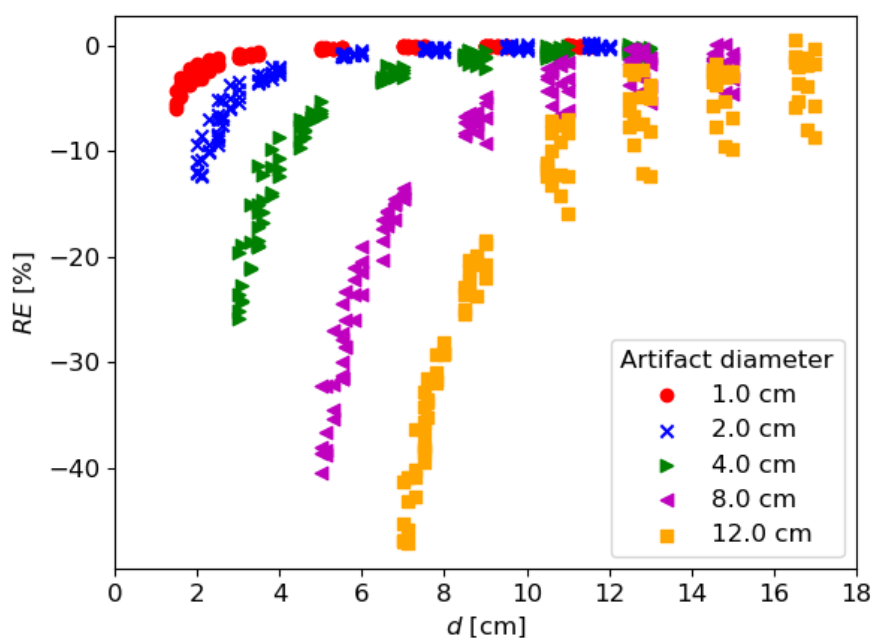


**Figure 4.1:**  $RE$  vs.  $d$  for the digital phantom experiment.

From the plot of  $RE$  versus  $d$  (figure 4.1), a clear inverse trend can be observed. Because  $d$  gives the distance between the center points of the artifact and tumors, data points from reconstructions with larger artifact diameters are shifted to the right.

To test the hypothesis that the  $RE$  would show a proportionality with  $1/d^2$ , the data shown in figure 4.1 was linearized, and an individual regression analysis was performed for data points obtained from reconstructions with the different artifact diameters. This was done in order to obtain the values for  $R^2$  and  $RMSE$ , describing the fit of the data to the regression lines. As can be observed in figure 4.2, the regression lines all show a good fit to the data, proven by the

high  $R^2$  values in table 4.1. The  $RMSEs$ , describing the standard error of the regression lines, increases with the artifact diameters, meaning the data points are more spread around the regression line for larger artifact diameters. This increased spread of data points is better visible in figure 4.1.

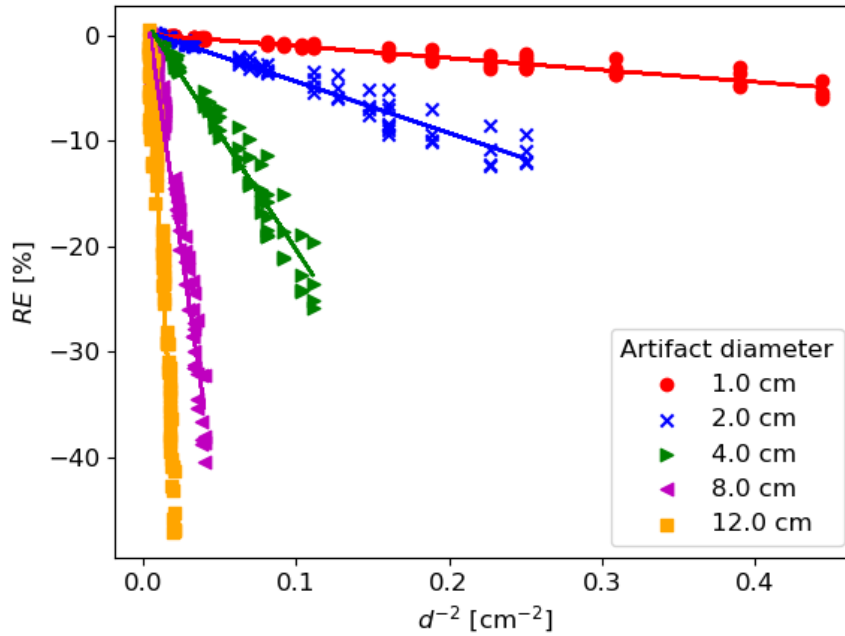
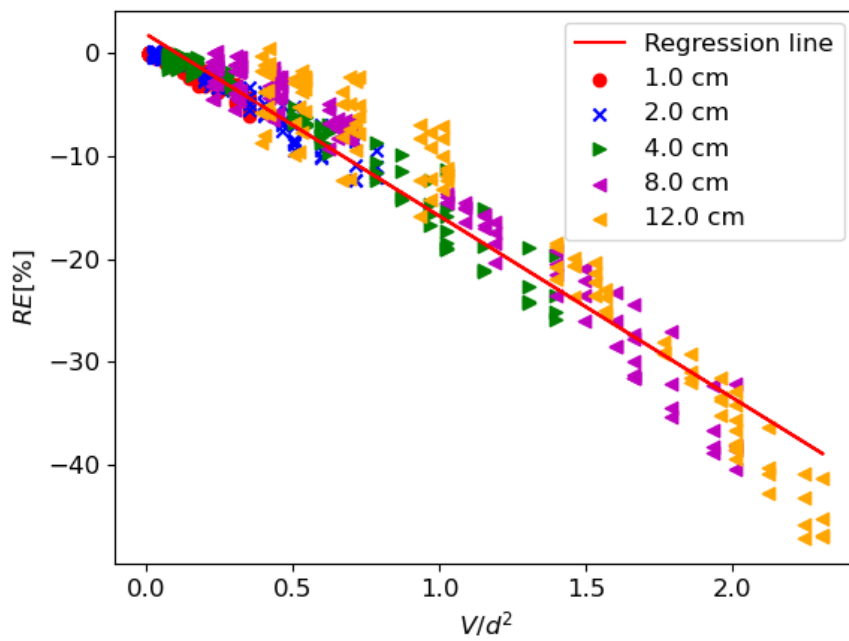


Figure 4.2:  $RE$  vs.  $d^{-2}$  for the digital phantom experiment.

Table 4.1: Parameters measuring the goodness of fit for regression lines in figure 4.2.

Artifact diameter [cm]	$R^2$	$RMSE$ [%]
1.0	0.9482	0.3
2.0	0.9606	0.7
4.0	0.9635	1.4
8.0	0.9640	2.3
12.0	0.9502	3.2

Because the  $RE$  was expected to have a linear relationship with  $V$  [18] and showed a proportionality with  $1/d^2$ , a regression analysis was also performed on the dataset in figure 4.1 with the ratio  $V/d^2$  as explanatory variable. The purpose of this was to see if we could obtain a linear equation describing the  $RE$  using only  $V$  and  $d$ :  $RE = a V/d^2 + b$ . The results from this analysis is visualized in figure 4.3, where data points are plotted, grouped as before, with the regression line. The values describing the fit of the model are  $R^2 = 0.9461$  and  $RMSE = 2.5\%$ .



**Figure 4.3:**  $RE$  vs.  $V/d^2$  for the digital phantom experiment.



### Reconstructions on the patient dataset

A similar analysis as that done on the digital phantom data was also conducted for the patient dataset, where simulated tumors and artifacts had been introduced (section 3.1.4). This was to investigate if the findings from the digital phantom in the previous section would also be valid for a real patient with a realistic activity distribution, i.e. where the activity distribution was less homogeneous.

Because the information along common LORs of an artifact and a tumor was assumed to have a significant impact on the  $RE$ , two situations were considered. In the first, individual reconstructions were run for a tumor placed at different distances from the artifact along a line. For each reconstruction, the tumor thus had similar information along the common LORs with the artifact. In the second, the tumors common LOR information with the artifact was randomized by randomly placing it around the artifact location. In figures from this analysis, we have also included a black dashed line which indicates the relevant error ( $\Delta_{sig}$ ) computed from equation (3.13). The relevant error was found to be  $\Delta_{sig} = -5.7\%$ . Data points *below* this line have errors that can be considered relevant.

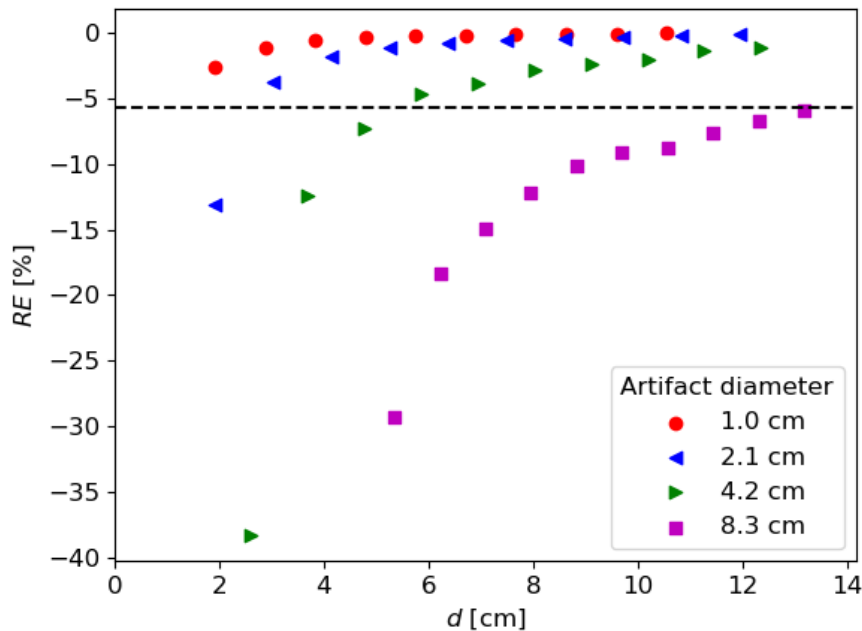
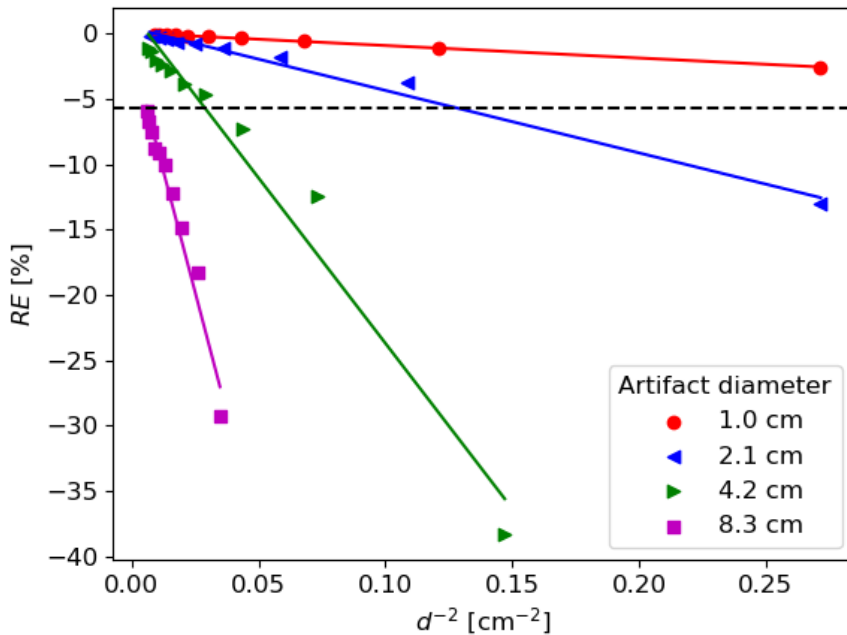


Figure 4.4:  $RE$  vs.  $d$  for the patient dataset. Tumor placed along line.

**Table 4.2:** Tabulated values of  $RE$  [%] observed in figure 4.4. Any  $RE \leq \Delta_{sig}$  is marked with an asterisk.

Artifact diameter	1.0 cm		2.1 cm		4.2 cm		8.3 cm	
	$RE$	$d$	$RE$	$d$	$RE$	$d$	$RE$	$d$
	-2.5	1.9	-13.1*	1.9	-38.3*	2.6	-29.3*	5.4
	-1.1	2.9	-3.7	3.0	-12.4*	3.7	-18.3*	6.2
	-0.6	3.8	-1.8	4.1	-7.2*	4.8	-14.8*	7.1
	-0.3	4.8	-1.1	5.3	-4.7	5.6	-12.1*	8.0
	-0.2	5.8	-1.8	6.4	-3.8	6.9	-10.1*	8.8
	-0.2	6.7	-0.6	7.5	-2.8	8.0	-9.2*	9.7
	-0.1	7.7	-0.5	8.6	-2.4	9.1	-8.7*	10.6
	-0.1	8.6	-0.4	9.7	-2.0	10.2	-7.6*	11.4
	-0.1	9.6	-0.2	10.8	-1.4	11.3	-6.8*	12.3
	-0.0	10.5	-0.1	11.9	-1.2	12.3	-5.9*	13.2

As can be observed in figure 4.4, when common LOR information is considered the  $RE$ s show the same inverse trend with  $d$  as we saw for the digital phantom experiment (figure 4.1). The  $RE$ s in figure 4.4 are also given in tabulated value (4.2).



**Figure 4.5:**  $RE$  vs.  $d^{-2}$  for the patient dataset. Tumor placed along line.

The analysis performed on the linearized data of figure 4.4 show that the regression lines have a good fit to the data (figure 4.5), proven by the high  $R^2$  in table 4.3. Here, the  $RMSE$  does not strictly increase with the artifact diameter.

**Table 4.3:** Parameters measuring the goodness of fit for regression lines in figure 4.5.

Artifact diameter [cm]	$R^2$	$RMSE$ [%]
1.0	0.9986	0.0
2.1	0.9855	0.5
4.2	0.9665	0.2
8.3	0.9709	1.2

The regression analysis performed on the data with  $V/d^2$  as explanatory variable also show a good fit to the obtained regression line, with  $R^2 = 0.9636$  and  $RMSE = 1.5\%$  (figure 4.6)

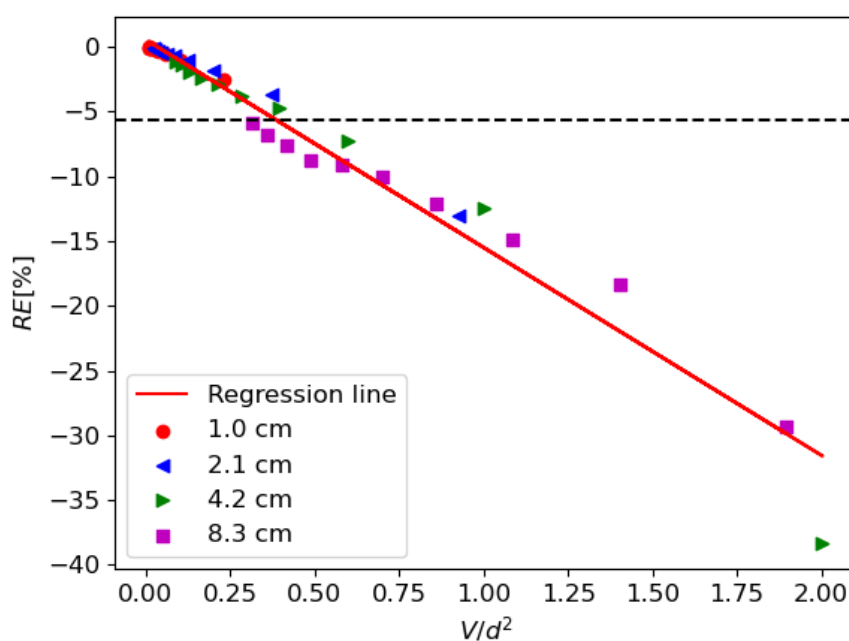


**Figure 4.6:**  $RE$  vs.  $V/d^2$  for the patient dataset. Tumor placed along line.

For the situation when the tumor were randomly placed around the location of the artifacts, the analysis was less conclusive.

Figure 4.7 shows the  $RE$  versus  $d$  for this situation. The tabulated values of figure 4.7 are also given (table 4.4). Interestingly, several tumors are not assigned relevant errors at distances which they were in the prior situation.

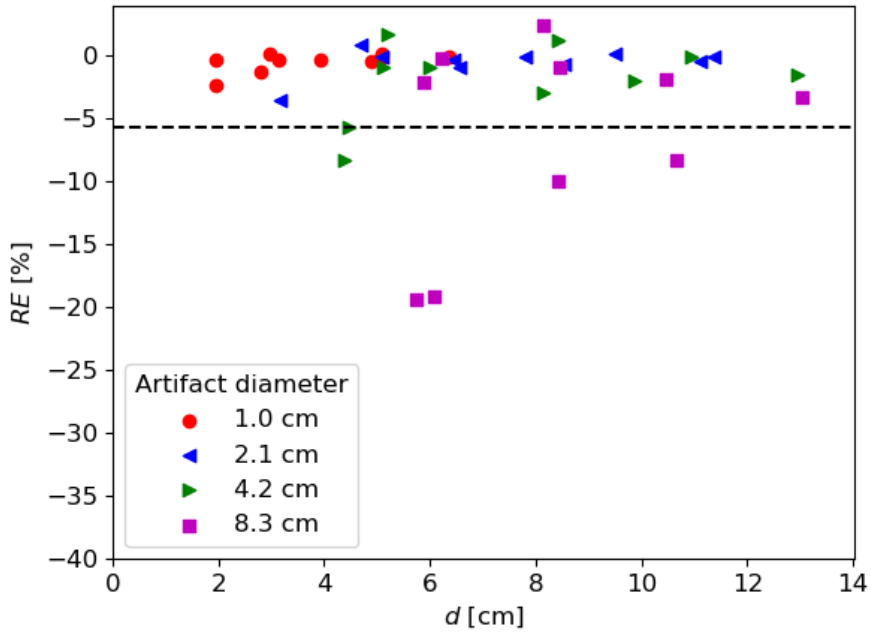


Figure 4.7:  $RE$  vs.  $d$  for the patient dataset. Random placement of tumors.

Table 4.4: Tabulated values of  $RE$ s observed in figure 4.7. Any  $RE \leq \Delta_{sig}$  is marked with an asterisk.

Artifact diameter	1.0 cm		2.1 cm		4.2 cm		8.3 cm	
	$RE$	$d$	$RE$	$d$	$RE$	$d$	$RE$	$d$
	-0.4	1.9	-3.5	3.1	-8.3*	4.4	-19.3*	5.8
	-2.4	2.0	-0.9	4.7	-5.7*	4.5	-2.1	5.9
	-1.3	2.8	-0.1	5.1	-0.9	5.1	-19.1*	6.1
	-0.2	3.0	-0.4	6.4	1.7	5.2	-0.3	6.2
	-0.3	3.1	-0.1	6.6	-0.9	6.0	2.4	8.2
	-0.3	4.0	-0.1	7.8	-2.9	8.1	-9.9*	8.4
	-0.4	4.9	-0.1	8.5	1.2	8.4	-0.9	8.5
	-0.2	5.0	-0.0	9.5	-2.0	9.9	-1.9	10.5
	-0.1	5.1	-0.0	11.1	-0.1	10.9	-8.3*	10.6
	-0.1	6.3	-0.0	11.4	-1.5	13.0	-3.3	13.0

The inverse trend observed previously (figure 4.5) is no longer present. This results in a bad fit of the regression lines (figure 4.8) to the data, indicated by the low  $R^2$  values and higher  $RMSE$  in table 4.5.

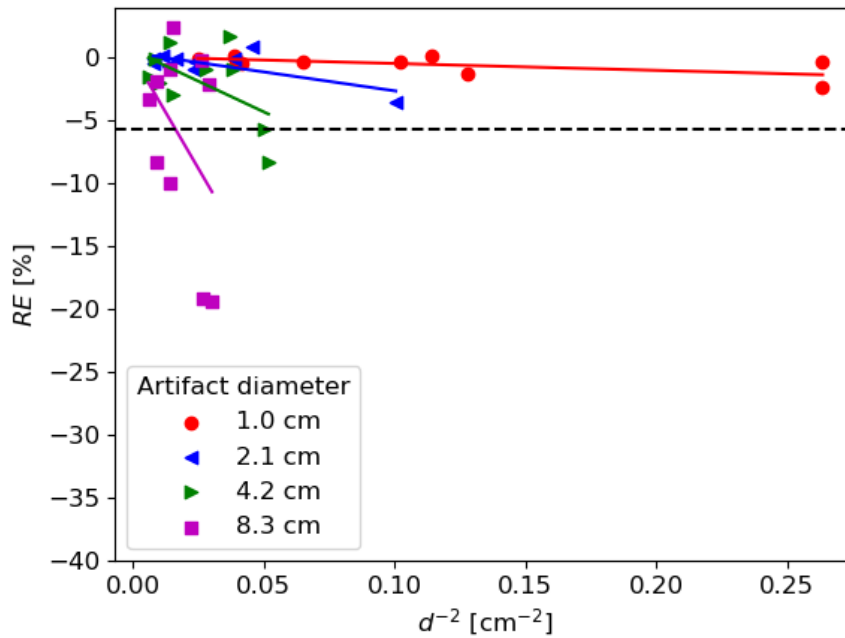


Figure 4.8:  $RE$  vs.  $d^{-2}$  for the patient dataset. Random placement of tumors.

Table 4.5: Parameters measuring the goodness of fit for regression lines in figure 4.8.

Artifact diameter [cm]	$R^2$	$RMSE$
1.0	0.4089	0.6
2.1	0.5235	0.8
4.2	0.3111	2.34
8.3	0.1797	2.40

Naturally, the regression line with  $V/d^2$  as explanatory variable also show a bad fit to the data. Figure 4.9 shows the regression line, with  $R^2 = 0.4098$  and  $RMSE = 3.6\%$ .

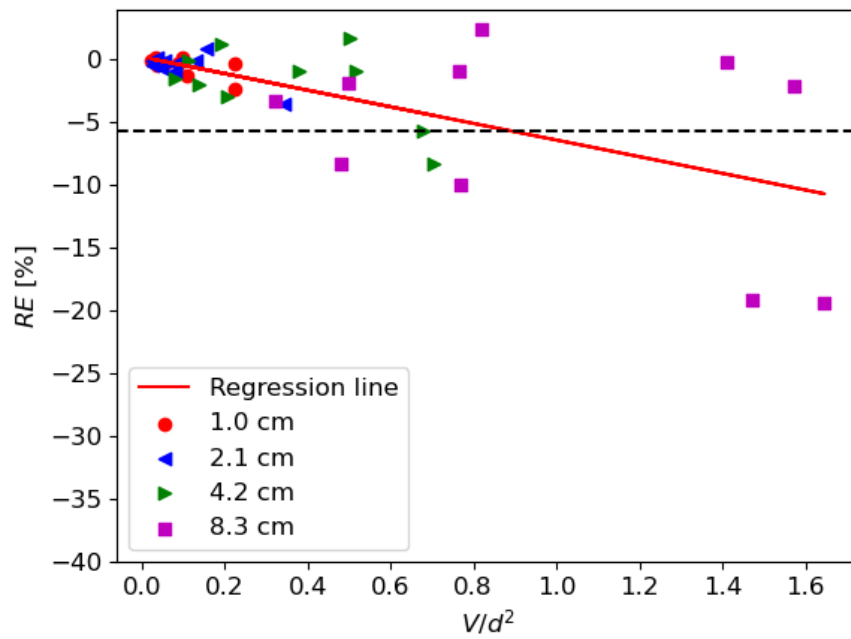
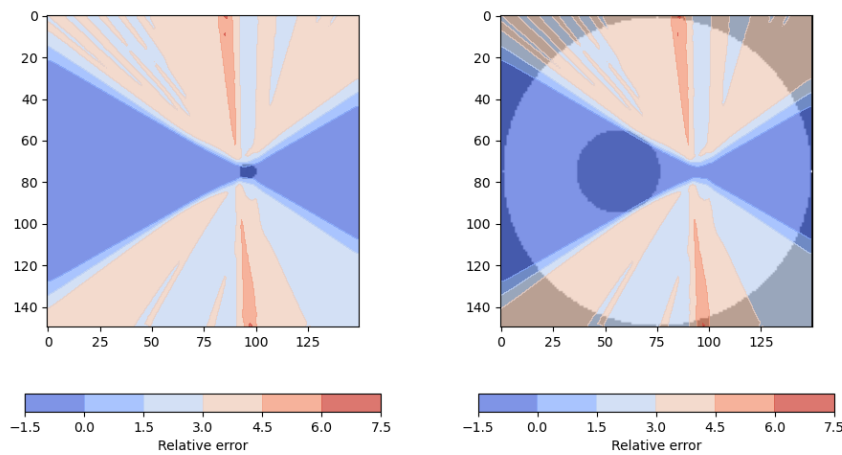


Figure 4.9: RE vs.  $V/d^2$  for the patient dataset. Random placement of tumors.

### 4.1.2 Effect of tumor activity

To study the effect of tumor activity in the presence of artifacts, reconstructions were run for the phantom setup as shown in figure 3.1, but with differing TBRs. Results are here presented as contour plots of the relative error from the reconstructed activity images according to equation (3.11).

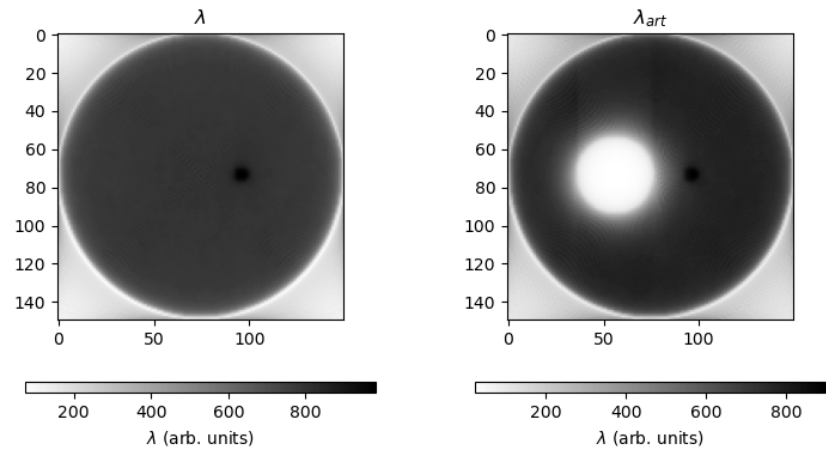
For the reconstruction of the noise free phantom setup, the contour plot of the relative error is overlaid on  $\lambda^*$ , containing the simulated tumor, and  $\mu_{art}$ , containing the artifact (figure 4.10). This indeed shows that underestimation of activity, indicated by dark blue areas, occurs on the common LORs. Interestingly, the underestimation of the attenuation values also lead to a strong positive bias in the vertical direction around the tumor.



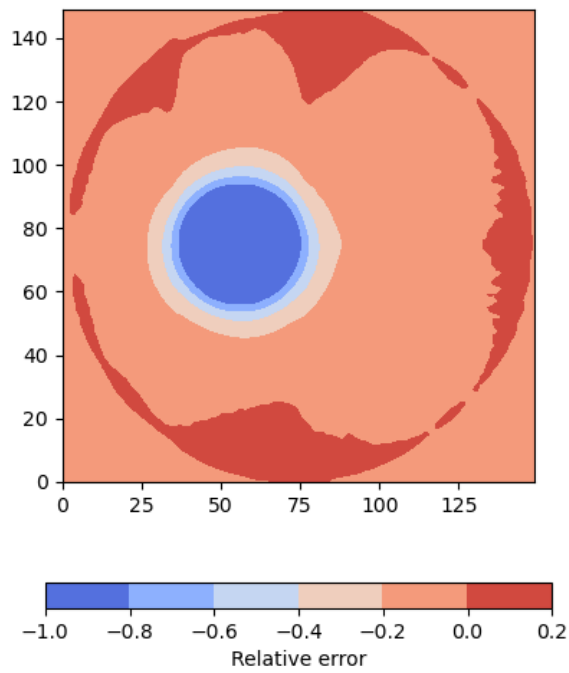
**Figure 4.10:** Contour plot of the relative error overlaid on  $\lambda^*$  (left) and  $\mu_{art}$  (right)

When background noise is present, the contour plots of the relative error show underestimation around the artifact location (figures 4.11 to 4.14). An important observation to be made is that, for increasing TBR, the error propagates further in the direction of the simulated tumor, i.e. in directions of higher activity.

For the following figures (4.11 to 4.14), subfigures **(a)** show the reconstructions with  $\mu$  and  $\mu_{art}$ , denoted  $\lambda$ ,  $\lambda_{art}$ . Subfigures **(b)** show the contour plot of the relative error between  $\lambda$ ,  $\lambda_{art}$ .



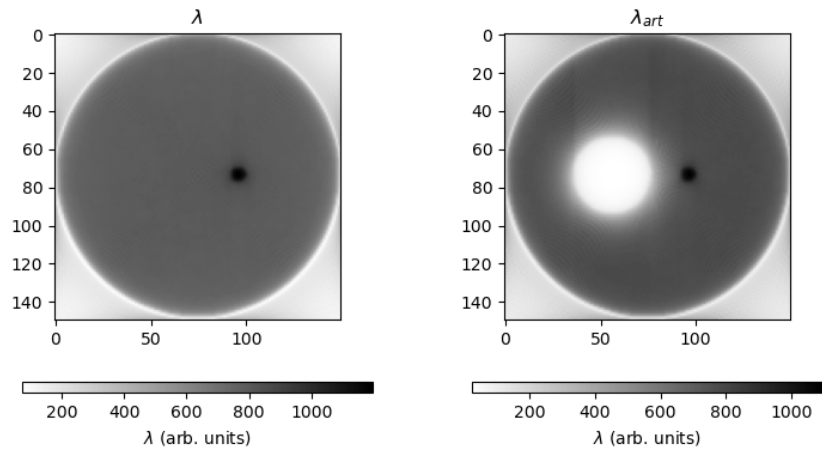
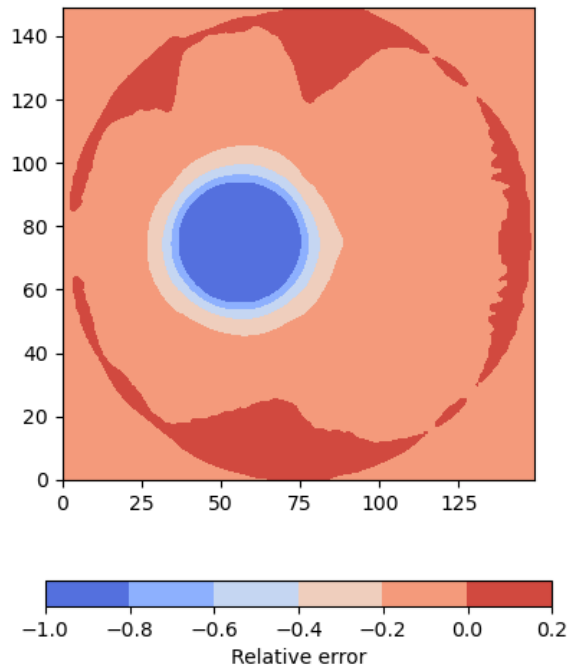
(a) Reconstructions with  $\mu$  (left) and  $\mu_{art}$  (right)



(b) Contour plot of the relative error of reconstructions in figure 4.11a

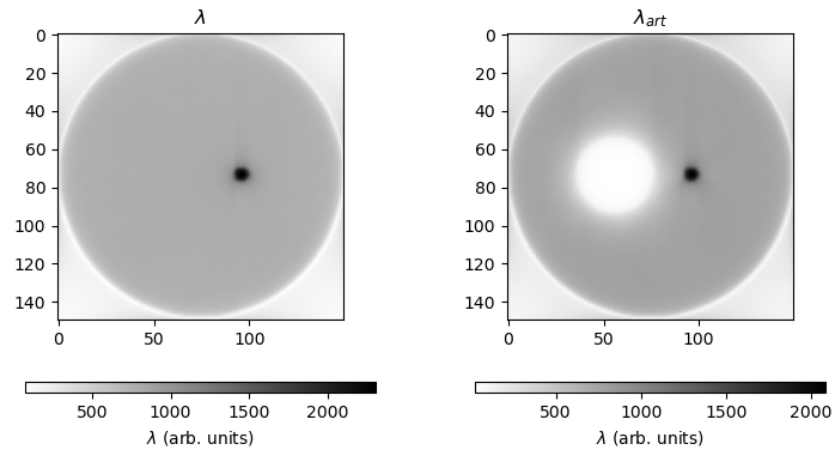
**Figure 4.11:** Illustration of the error of phantom reconstructions with TBR=1.5



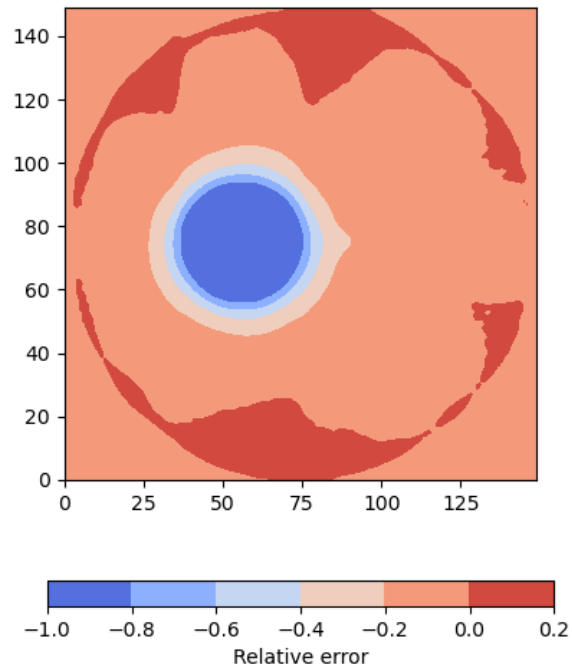
(a) Reconstructions with  $\mu$  (left) and  $\mu_{art}$  (right)

(b) Contour plot of the relative error of reconstructions in figure 4.12a

**Figure 4.12:** Illustration of the error of phantom reconstructions with TBR=2

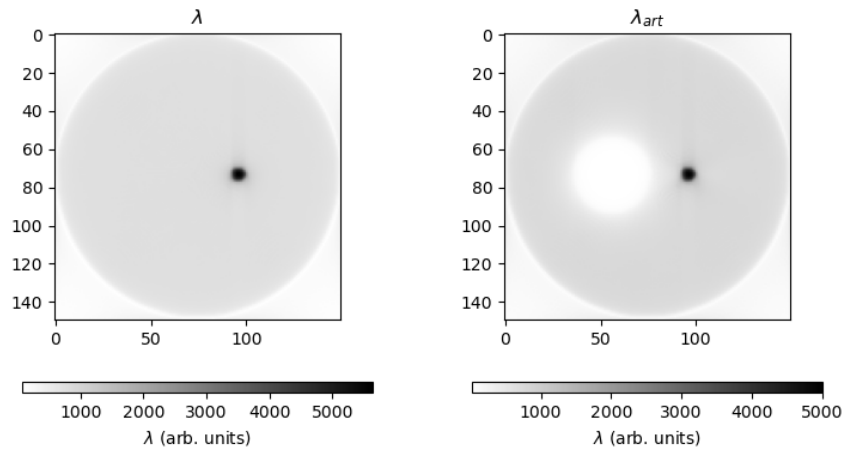


(a) Reconstructions with  $\mu$  (left) and  $\mu_{art}$  (right)

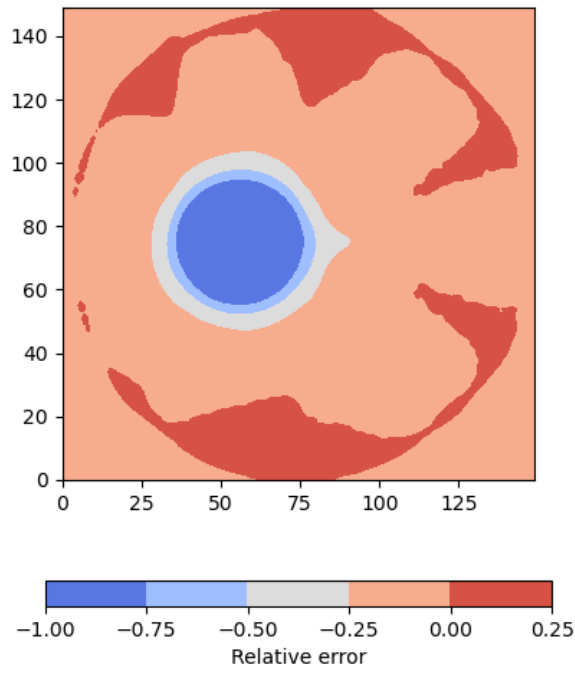


(b) Contour plot of the relative error of reconstructions in figure 4.13a

**Figure 4.13:** Illustration of the error of phantom reconstructions with TBR=4



(a) Reconstructions with  $\mu$  (left) and  $\mu_{art}$  (right)



(b) Contour plot of the relative error of reconstructions in figure 4.14a

**Figure 4.14:** Illustration of the error of phantom reconstructions with TBR=8

## 4.2 Performance of correction method

Here, the performance of the proposed method for correcting voxels that wrongly has been assigned the attenuation value of lung tissue (section 3.2.1) is presented. The artifact was synthetically introduced into the 3-D attenuation map of the patient data we used for the previous study, as illustrated in figure 3.8.

From the 3-D attenuation map containing the artifact, we extracted a 3-D boolean mask of all voxels that had been assigned the attenuation value of lung tissue. With this mask, histograms of the intensity values of voxels in the corresponding 3-D opposed-phase Dixon image were created. Figure 4.15 shows the histograms obtained from opposed-phase images with different liver signal intensities, as illustrated in figure 3.9. We observe two distinct classes on each of these histograms, and the threshold obtained from performing Otsu's method. This shows that a valid threshold can be obtained, even for lowered liver signal intensities on the opposed-phase images, allowing us to separate liver tissue from lung tissue.

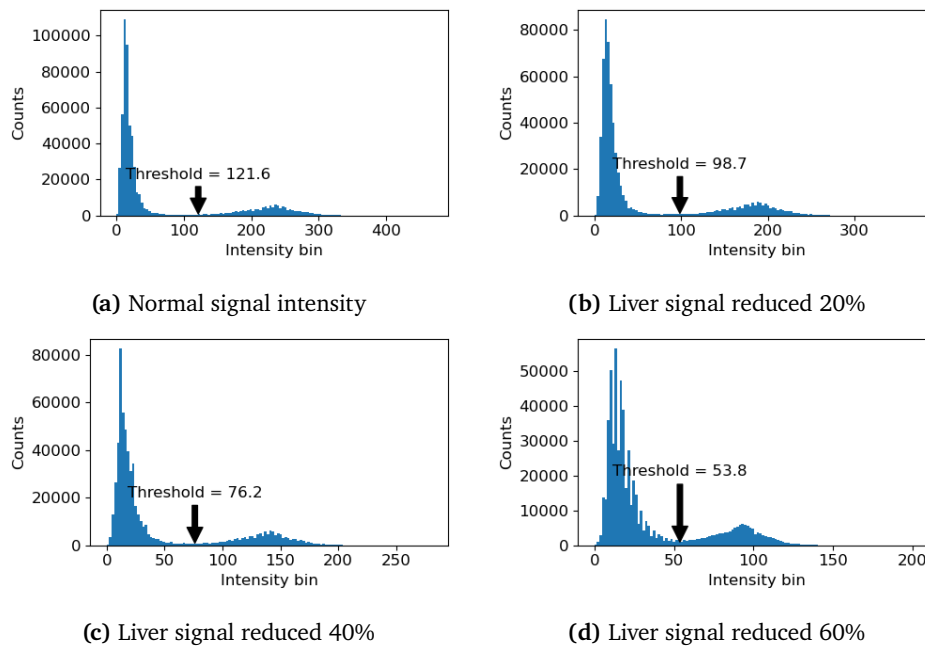


**Figure 4.15:** Histograms for intensity values of voxels.

By inspection of the histograms in figure 4.15, we observe two distinct classes. The class corresponding to lung voxels is in the lower intensity range, and the class corresponding to soft/liver tissue is in a higher intensity range. As the signal intensity in the liver decreases, naturally, the threshold obtained from

Otsu's method decreases.

To evaluate the performance of the correction method, the percentage of correctly changed liver voxels in the attenuation map with artifact was computed. The percentage of lung voxels that were incorrectly changed was also included (table 4.6). The performance was assessed for several different liver signal intensities on the opposed-phase image.

**Table 4.6:** Performance of correction method for different liver signal intensities in the opposed-phase images.

Liver signal	Liver[%]	Lung[%]
100%	96	0
90%	96	0
80%	96	0
70%	96	0
60%	96	0
50%	96	1
40%	95	1
30%	94	3
20%	93	10
10%	75	31

To visually illustrate the performance on the attenuation map, figure 4.16 shows the result of the correction algorithm for the same coronal slice as in figure 3.8. This illustration is created with normal liver signal intensity on the opposed-phase image. Small areas at the lower border of the liver and the adjoining tissue can be seen where the algorithm has not been able to correct the attenuation values.

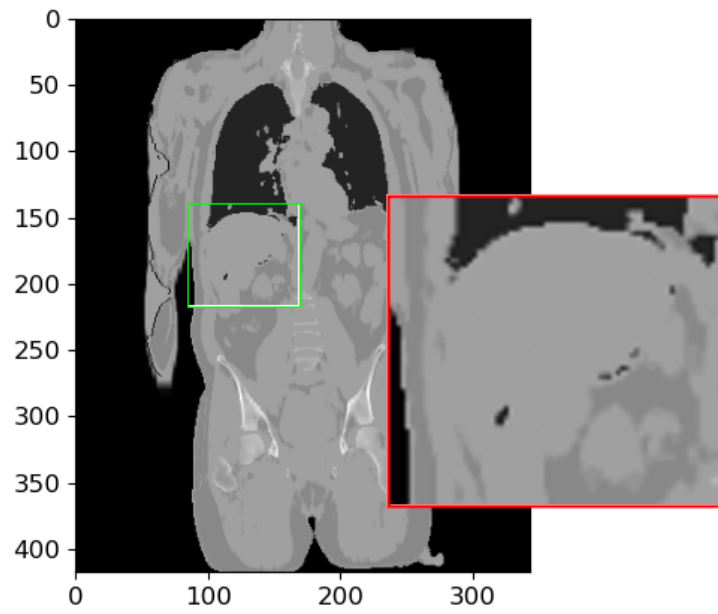


**Figure 4.16:** Performance of correction method illustrated for the same coronal slice as in figure 3.8.

# /5

## Discussion

Here, we will discuss the results presented in chapter 4, starting with the findings on the impact of susceptibility artifacts on adjacent tumors. Thereafter, the proposed correction method will be evaluated.

### 5.1 Misclassifications in segmented MRAC

The results showed that relevant errors ( $RE \leq \Delta_{sig} = -5.7\%$ ) can be introduced to tumors adjacent to the artifacts, even if only a part of the liver is misclassified. In general, artifacts of diameter 1 cm did not show relevant errors at any tumor-artifact distance,  $d$ , (tables 4.2 and 4.4), but for larger artifact diameters, correction methods are needed. However, the  $d$  at which an artifact of a given diameter caused  $RE \leq \Delta_{sig}$  varied, even for similar tumor-artifact distances,  $d$ . This is particularly interesting, and may be explained by the effect of common LOR information.

By considering the setups of artifact diameter 8.3 cm (figures 3.5 and 3.6), i.e. when common LOR information of each tumor was similar and random with the artifact, an interesting observation can be made. In the first case (figure 3.5), the tumors will, in general, have much activity and attenuating material along the common LORs with the artifact. This is due to the position of the tumors relative to the artifact. In anatomical terms, they are located in a more *lateral* direction relative to the artifact. In the latter case (figure 3.6), several tumors are located

more in the *anterior* direction, and thus have less activity and attenuating material along the common LORs with the artifact. From the digital phantom experiments, it became clear that larger errors could be expected in directions of high activity (section 4.1.2). In addition, as was pointed out by Berker and Li [34], the same is true for directions of high attenuation. This means that, due to the ellipse-like shape of the patients upper body, tumors located in the more anterior direction relative to the artifact should suffer less error. The opposite is then true for tumors located in a more lateral direction. The suggestion therefore is that the tumors located in a more anterior direction relative to the artifact are the ones that do not get assigned relevant errors in the cases where tables 4.2 and 4.4 disagree. This is a subject that should be further investigated. An isolated study on the effect of attenuation was not done in this thesis, but the effect of attenuation along common LORs should also be further studied. If more attenuation leads to larger PET quantification errors in segmented MRAC images with misclassifications, then areas where, for example, much bone is present, or in the attenuation map of overweight patients, quantification errors should be larger due to the increased attenuation.

Another interesting observation that can be made from table 4.4 is that, in a few cases,  $RE > 0$ . This contradicts what was found in the phantom study [18], i.e. that wrongly assigning a lower attenuation value to a tissue type should cause *underestimation* of the activity. Positive bias is also present on the contour plots from the digital phantom experiment (figures 4.11 to 4.14). It has been observed that the OSEM reconstruction algorithm overestimates the activity concentrations in low count regions [52, 53], which can explain this. The OSEM algorithm has an inherent non-negativity constraint, to accommodate the physical non-negativity of photon attenuation [32]. However, the strong positive bias we observe in the vertical direction on the contour plots is harder to explain, and has been observed previously [54, 55]. As the Radon space is closely related to the Fourier frequency space through the central slice theorem [33], an assumption is that the step function-like decrease in attenuation caused by the artifact introduces this, but this was not further investigated in this thesis.

The observation that the error propagates further in the direction of higher activity from figures 4.11 to 4.14 is important. It shows that activity distribution must be considered in the evaluation of PET/MRI images with artifacts present. In the case where a tissue type is wrongly assigned a lower attenuation value, particular care must be taken. A tumor located between an artifact and an area of high activity accumulation can potentially suffer a larger quantification error, which in the worst case can leave it impossible to detect. For  $^{18}\text{F}$ -FDG examinations, high activity accumulation can be seen in the brain, heart, kidneys and urinary tract [56]. Therefore, tumors around these organs may suffer larger errors in the presence of segmentation errors in the MRAC images.



The method used in this thesis should be considered experimental, and it is not sure if the exact same errors would be observed if reconstructions were done on a PET/MRI machine. Both because the assumption of using reconstructed, thus processed, PET/MRI images as ground truth images is weak, and also due to the multiple reconstruction parameters and pre-/post-processing steps that were not considered in this thesis. In addition, here, the reconstructions were done on 2-D image slices, whereas e.g. the Siemens Biograph mMR has the capability to do reconstructions on 3-D sinograms. This means a tumor and an artifact can have 3-D common LORs. However, the results from using 2-D circular artifacts may be considered as a worst case scenario for 3-D *spherical* artifacts of equal diameters. Obviously, the shape of an artifact will influence the errors. Here, we have considered circular shapes, but it would have been interesting to see the effect of, e.g., ellipse-shaped artifacts with different widths and heights. This may provide insight in whether it is better (worse) to have more (fewer) common LORs, but less (more) misclassification along common LORs. Again, as circular artifacts were considered here, the results can be considered a worst case for elliptical misclassifications of similar semi-major axis diameters for the  $d$ s considered. Furthermore, the results are based on the analysis of only *one* patient. Therefore, no generalizations should be made from the results regarding at which  $d$  a relevant error occurs. As we have seen, the errors can be expected to vary depending on activity and attenuation, which, between different patients, also varies. Still, the main purpose of this thesis was not to accurately quantify the errors, but rather to study the more general implications of susceptibility artifacts, and especially, how the error behaved with respect to  $d$ . This was the main reason for using data from only one patient.

By considerations of the inverse square law,  $d$  was expected to have an inverse square relationship with the  $RE$ . By logical reasoning, the annihilation photons from a tumor that passes an artifact also obey the inverse square law, and can thus be directly related to the number of common LORs. Assuming similar information along the common LORs, the results showed the hypothesis to be true, indicated by the high  $R^2$  values of the regression lines in tables 4.1 and 4.3. However, this was only tested for tumors placed in regions of homogeneous uptake. When comparing the  $R^2$  values of tables 4.1 and 4.3, we see a better fit for regression lines belonging to the patient dataset. As we did reconstructions with only one TBR and tumor size, this dataset has less variation which resulted in a better fit.

The  $RE$  was also expected to be proportional with  $V$  [18]. Therefore, the attempt was made to see if the ratio  $V/d^2$  could explain the  $RE$ . If a linear equation  $RE = a \cdot V/d^2 + b$  may be obtained, this could serve as a quick and easy-to-use tool to judge whether artifacts of a given  $V$  causes a relevant error on an adjacent tumor. From geometrical considerations, artifact size, tumor size

and the distance between the tumor and artifact are all factors determining the *number* of common LORs. Relating these three factors essentially boils down to a geometrical problem. Here, the fact that we were working with (2-D) extended sources, not point sources which the inverse square law applies to, was neglected. Although a relationship with tumor size was not obtained, figures 4.3 and 4.6 both show a good fit with the regression line ( $R^2 = 0.964$  and  $0.9636$ , respectively). If a relationship with tumor size is obtained, a better fit can be assumed. The regression line obtained from the case where information along the common LORs was random showed a bad fit to the data, with  $R^2 = 0.4098$ , and a large spread of data points around the line ( $RMSE = 3.58\%$ ). This means a generalized linear model cannot be obtained using only the ratio  $V/d^2$  to describe the errors. Regardless, this is a promising result showing that there may be value in grouping the tumors on lines/in sectors when studying the errors induced by susceptibility artifacts. In areas of the body where susceptibility artifacts occur more frequently, e.g. around common locations of metal implants, such as hip prosthesis, dental implants or metal wires in the sternum [17], this may be used as a basis for further studies. The results show that, for tumors with similar common LOR information, a linear equation  $a \cdot V/d^2 + b$  may be obtained to predict at what distance  $RE \geq \Delta_{sig}$  for a given artifact diameter. By solving the inequality for  $d$ , we get:

$$RE \geq \Delta_{sig} \quad (5.1)$$

$$a V/d^2 + b \geq \Delta_{sig} \quad (5.2)$$

$$d \geq \sqrt{\frac{a \cdot V}{\Delta_{sig} - b}}, \quad (5.3)$$

which would have been most interesting to test if more data was available. However, if such a model can be obtained, more uncertainty can be expected for larger artifact diameters, judging from the strictly increasing  $RMSE$  for the regression lines obtained from the digital phantom experiment 4.1.

Ladefoegd et. al [54] has previously conducted a study on dental artifacts in the head and neck region. They found that changes in  $SUV_{mean}$  following correction for dental artifacts was largest near the signal void, and that differences decreased in regions further away. This can be explained by our finding that the error propagates as the inverse square of the distance. Ladefoegd et. al also stated that "The effect of the artifact decreased with the distance to the signal void in a non-simple pattern...". From the work conducted here, we have seen that this "non-simple" pattern depends on the activity distribution, and should also have a dependency on attenuation [34].

In a study on the effect of susceptibility artifacts related to metallic implants on adjacent lesions by Svirydenka et. al [17], only a weak inverse correlation between tumors affected by artifacts and distance was found. Here, it has been shown that a  $1/d^2$  can be obtained by taking common LOR information into consideration. Svirydenka et. al also observed that the errors outside the artifacts propagated in a "fan-shaped fashion". The findings in this thesis, i.e. that larger errors can be expected in directions of high activity, can also explain this.

## 5.2 Correction method

The devised correction method used information from the (3-D) opposed-phase Dixon images to correct misclassified liver voxels. The method does not require any manual steps or special software to function and, most importantly, guarantees perfect anatomical matching. Compared to previously suggested methods for susceptibility artifact correction, this has several benefits. By utilizing already acquired data, no extra scanning time is required for dedicated MR sequences to image tissues with short  $T_2^*$  relaxation time. This is a limitation of UTE-based approaches [7]. Other approaches, such as atlas based methods, require a reliable and locally precise intersubject registration. This can be hard to obtain because of high intersubject variability, which gives need for large patient atlas databases [24]. Time consumption is also an issue with atlas based methods, due to the computationally intensive image registration between the atlases and target MRI volumes [7].

The results (table 4.6) show that the proposed method were able to correct 96% of misclassified voxels without changing the value of any lung pixels for a liver signal reduction down to 50% in the opposed-phase image. After this, the algorithm performed increasingly worse. By inspection of the histograms in figure 4.15, we see that if the signal is too low, classes will eventually overlap which makes them harder to discriminate. A small overlap between the classes can be observed in figure 4.15d. When this occur, the algorithm will not be able to discriminate all voxels correctly which leads to the false assignment of soft tissue attenuation values to lung voxels and vice versa. The proposed method thus requires sufficient signal from the liver to be able to separate the classes. Here, it was found that 50% of normal signal intensity from the liver is required in order to work without mixing classes. It is not obvious if this is valid in every case, as the analysis is based on the results of only one patient. It is neither not easy to say for which iron loads or  $T_2^*$ -reductions we obtain sufficient signal from the liver. If iron loads are very high and the  $T_2^*$  is very short, the devised method might not work. However, none of the reported cases [10, 11, 12] where the misclassification of liver tissue as lung tissue occurred

have shown any substantial signal loss from the liver in the opposed-phase MR images. Therefore, the method is promising.

In figure 4.16 it was seen that the algorithm was not able to correct small areas at the border of the liver. As explained in section 2.1.2 on "Tissue Contrast and Magnetic Susceptibility", small differences in the magnetic properties of adjoining tissues degrade the homogeneity of the external magnetic field. These inhomogeneities further affect the relaxation of the tissues, speeding up the apparent spin-spin relaxation times  $T_2^*$ , explaining why we get lower signal intensity on the borders of the organ. Therefore, these voxels fall below the threshold and are not corrected. Morphological dilation can be used to correct for this, but then we run into the risk of assigning the wrong attenuation values in other areas. This might not, however, be a large problem. As discussed in the previous section, small misclassifications may not introduce relevant errors, especially if a tumor is located far away from the artifact.

### 5.3 Summary

In this thesis, the impact of susceptibility artifacts on adjacent tumors have been investigated through simulated tomography experiments. In particular, the consequences of misclassification of liver (soft) tissue as lung tissue was examined. These artifacts can occur from iron overload in the liver due to faster  $T_2^*$  spin dephasing that occur when iron substances is present in tissue. This in turn presents as a signal loss in the areas of high iron accumulation on the acquired MR-images, which lead to errors in the creation of attenuation maps. Because the liver is a major storage for iron in the human body, this organ is especially exposed for susceptibility artifacts. This can lead to the false assignment of liver tissue as lung tissue in the attenuation maps. Particularly, by causing the connected component analysis, meant for detecting lung tissue, to fail, thus making in unable to separate lung tissue from liver tissue. The artifacts did, in some cases, cause relevant underestimation ( $RE \leq 5.7\%$ ) on tumors adjacent to the artifact, which demonstrated the need for correction methods. A novel approach for correcting these types of artifacts was presented. The suggested method is based on using Otsu's method on the opposed-phase Dixon image for finding the best threshold to separate lung and liver voxels.

The question as to how large errors can be before they might influence diagnosis remains open. Our use of the relevant error as  $\Delta_{sig} = -5.7\%$  is not based on any visual interpretations, but rather errors that cannot be explained by image noise. However, being aware of the parameters that has the potential to increase errors is important. The findings that the  $RE$  show a proportionality  $d^2$ ,  $V/d^2$ , and reaches further in the directions of increased activity is also important, and

can be useful knowledge for radiographers and nuclear medicine radiologists in the evaluation of PET/MRI images with segmentation errors in the attenuation maps.



# /6

## Conclusion

Susceptibility artifacts presenting as misclassification of liver (soft) tissue as lung tissue in the attenuation maps used for AC in hybrid PET/MRI imaging may introduce relevant underestimation ( $\Delta_{sig} \leq -5.7\%$ ) on tumors adjacent to the artifact. This has been shown through computing the relative error (*RE*) of synthetic tumors introduced in a realistic PET/MRI patient dataset. The PET images were reconstructed from emission data acquired from simulated tomography experiments, for attenuation maps with and without synthetic artifacts in the patients liver. For reconstructions, the OSEM-algorithm was used.

The information along common LORs, i.e the activity and attenuation, of an artifact and a tumor have a large impact on the error caused by the artifacts. From contour plots describing the *RE* on the whole 2-D reconstructed images of a digital phantom, the underestimation caused by the artifacts were shown to extend further in directions of higher activity. It is also believed that the same is true for directions of high attenuation [34]. Here, due to the ellipse-like shape of the patients torso, this effect lead to tumors located in a more anterior/posterior direction relative to the artifact to suffer less error, because of the lower activity and attenuating material on the common LORs with the artifact. This is a topic that should further investigated.

Assuming similar common LOR information between a tumor and an artifact, the *RE* is proportional with the inverse square of the distance ( $d$ ) between the center points of the artifact and tumor. This was indicated by high  $R^2$  values

obtained from linear regression analysis on the  $RE$  obtained from reconstructed images with tumors  $a$  of the digital phantom (average  $R^2 = 0.9573$ ) and the patient dataset (average  $R^2 = 0.9804$ ).

Because the  $RE$  is also proportional to the volume ( $V$ ) of an artifact [18], a linear equation describing the  $RE$  may be obtained:  $RE = a \cdot V/d^2 + b$ . If sufficient data is obtained, this may be used to predict at which  $d$  we get  $RE \geq \Delta_{sig}$ :

$$\begin{aligned} RE &\geq \Delta_{sig} \\ a V/d^2 + b &\geq \Delta_{sig} \\ d &\geq \sqrt{\frac{a \cdot V}{\Delta_{sig} - b}}, \end{aligned}$$

which would be a quick and easy-to-use tool to find out when errors are too large to be acceptable.

A method for correcting lung-liver misclassifications in the attenuation map was also proposed. By using Otsu's method for thresholding on the opposed-phase image from a standard Dixon sequence, it was able to correct 96% of pixels down to 50% reduction in liver signal. The algorithm benefits from using already acquired data to correct the artifacts, and may be implemented in real-time.



# Bibliography

- [1] PhD Cherry Simon R. “Multimodality Imaging: Beyond PET/CT and SPECT/CT.” eng. In: *Seminars in nuclear medicine* 39.5 (2009), pp. 348–353. ISSN: 0001-2998.
- [2] Harald H Quick. “Integrated PET/MR.” eng. In: *Journal of magnetic resonance imaging* 39.2 (2014), pp. 243–258. ISSN: 1053-1807.
- [3] Adam M Alessio et al. “PET/CT scanner instrumentation, challenges, and solutions.” eng. In: *The Radiologic clinics of North America* 42.6 (2004), pp. 1017–1032. ISSN: 0033-8389.
- [4] Daniel H Paulus et al. “Towards integration of PET/MR hybrid imaging into radiation therapy treatment planning.” eng. In: *Medical physics (Lancaster)* 41.7 (2014), 072505–n/a. ISSN: 0094-2405.
- [5] Gaspar Delso and Sibylle Ziegler. “PET/MR System Design.” eng. In: 2014, pp. 1–19. ISBN: 3642406920.
- [6] Borjana Bogdanovic et al. “Almost 10 years of PET/MR attenuation correction: the effect on lesion quantification with PSMA: clinical evaluation on 200 prostate cancer patients.” In: *European Journal of Nuclear Medicine and Molecular Imaging* 48.2 (2021), pp. 543–553.
- [7] Ciprian Catana. “Attenuation correction for human PET/MRI studies.” eng. In: *Physics in medicine & biology* 65.23 (2020), 23TR02–23TR02. ISSN: 0031-9155.
- [8] “PET/MRI: Attenuation correction.” eng. In: 1st ed. 2018. Cham: Springer International Publishing : Imprint: Springer, 2018, pp. 53–77. ISBN: 3-319-68517-1.
- [9] Donald W McRobbie et al. *MRI from Picture to Proton*. eng. 2nd ed. Cambridge: Cambridge University Press, 2006. ISBN: 052168384X.
- [10] Robert Matthews et al. “Positron emission tomography-magnetic resonance liver parenchyma attenuation correction artifact in secondary hemochromatosis.” eng. In: *World journal of nuclear medicine* 19.1 (2020), pp. 85–88. ISSN: 1450-1147.
- [11] Florian Büther et al. “An artefact of PET attenuation correction caused by iron overload of the liver in clinical PET-MRI.” eng. In: *European journal of hybrid imaging* 1.1 (2017), pp. 1–6. ISSN: 2510-3636.
- [12] Ronald JH Borra et al. “Effects of ferumoxytol on quantitative PET measurements in simultaneous PET/MR whole-body imaging: a pilot

- study in a baboon model.” eng. In: *EJNMMI physics* 2.1 (2015), pp. 1–12. ISSN: 2197-7364.
- [13] Herbert L. Bonkovsky. “Iron and the Liver.” In: *The American Journal of the Medical Sciences* 301.1 (1991), pp. 32–43. DOI: 10.1097/00000441-199101000-00006.
- [14] S Holm et al. “Image Distortions in Clinical PET/MR Imaging.” eng. In: *PET/MRI : Methodology and Clinical Applications*. 2014, pp. 21–41. ISBN: 3642406920.
- [15] Soo Jin Bae et al. “Iron Overload during Follow-up after Tandem High-Dose Chemotherapy and Autologous Stem Cell Transplantation in Patients with High-Risk Neuroblastoma.” eng. In: *Journal of Korean medical science* 27.4 (2012), pp. 363–369. ISSN: 1011-8934.
- [16] Resonance Health. *Iron Overload in Cancer Survivors*. URL: <https://www.resonancehealth.com/news/20-products/ferriscan/161-iron-overload-in-cancer-survivors.html>.
- [17] Hanna Svirydenka et al. “The effect of susceptibility artifacts related to metallic implants on Adjacent-Lesion assessment in simultaneous TOF PET/MR.” In: *Journal of Nuclear Medicine* 58.7 (2017), pp. 1167–1173.
- [18] Erlend Bredal Olsen. “Susceptibility artifacts in PET/MRI.” In: (2020).
- [19] Vincent Keereman et al. “The effect of errors in segmented attenuation maps on PET quantification.” In: *Medical physics* 38.11 (2011), pp. 6010–6019.
- [20] Claes Nøhr Ladefoged et al. “Impact of incorrect tissue classification in Dixon-based MR-AC: fat-water tissue inversion.” In: *EJNMMI physics* 1.1 (2014), pp. 1–9.
- [21] Kirsten Nunez. *Largest Organ in the Body: Size, Weight & Interesting Facts*. Feb. 2020. URL: <https://www.healthline.com/health/largest-organs-in-the-body>.
- [22] Ilja Bezrukov et al. “MR-Based Attenuation Correction Methods for Improved PET Quantification in Lesions Within Bone and Susceptibility Artifact Regions.” eng. In: *The Journal of nuclear medicine (1978)* 54.10 (2013), pp. 1768–1774. ISSN: 0161-5505.
- [23] Claes Nøhr Ladefoged et al. “PET/MR imaging of the pelvis in the presence of endoprostheses: reducing image artifacts and increasing accuracy through inpainting.” In: *European journal of nuclear medicine and molecular imaging* 40.4 (2013), pp. 594–601.
- [24] Matthias Hofmann et al. “MRI-Based Attenuation Correction for PET/MRI: A Novel Approach Combining Pattern Recognition and Atlas Registration.” eng. In: *The Journal of nuclear medicine (1978)* 49.11 (2008), pp. 1875–1883. ISSN: 0161-5505.
- [25] Trisha L Roy et al. “MRI for peripheral artery disease: Introductory physics for vascular physicians.” In: *Vascular Medicine* 23.2 (2018), pp. 153–162.

- [26] Simone Mastrogiacomo et al. “Magnetic resonance imaging of hard tissues and hard tissue engineered bio-substitutes.” In: *Molecular imaging and biology* 21.6 (2019), pp. 1003–1019.
- [27] F Bloch. “Nuclear Induction.” eng. In: *Physical review* 70.7-8 (1946), pp. 460–474. ISSN: 0031-899X.
- [28] Anup S Shetty et al. “In-phase and opposed-phase imaging: applications of chemical shift and magnetic susceptibility in the chest and abdomen.” In: *Radiographics* 39.1 (2019), pp. 115–135.
- [29] Simon R Cherry and Magnus Dahlbom. *PET: Physics, Instrumentation, and Scanners*. eng. New York, NY: Springer New York. ISBN: 0387323023.
- [30] Rachel A Powsner, Matthew R Palmer, and Edward R Powsner. *Essentials of Nuclear Medicine Physics and Instrumentation*. eng. Somerset: John Wiley & Sons, Incorporated, 2013. ISBN: 9780470905500.
- [31] Ignasi Carrio and Pablo Ros. *Pet/mri: Methodology and Clinical Applications*. eng. 2014th ed. Berlin, Heidelberg: Springer Berlin / Heidelberg, 2013. ISBN: 3642406912.
- [32] H.M Hudson and R.S Larkin. “Accelerated image reconstruction using ordered subsets of projection data.” eng. In: *IEEE transactions on medical imaging* 13.4 (1994), pp. 601–609. ISSN: 0278-0062.
- [33] Timothy G Feeman. *The Mathematics of Medical Imaging: A Beginner’s Guide*. eng. 2nd ed. 2015. Springer Undergraduate Texts in Mathematics and Technology. Cham: Springer International Publishing. ISBN: 9783319226644.
- [34] Yannick Berker and Yusheng Li. “Attenuation correction in emission tomography using the emission data—A review.” eng. In: *Medical Physics* 43.2 (2016), pp. 807–832. ISSN: 0094-2405.
- [35] Thomas Hope, Andrei Iagaru, and Patrick Veit-Haibach. *Pet/mri in Oncology: Current Clinical Applications*. eng. Springer International Publishing, 2018. ISBN: 9783319685168.
- [36] Rafael C Gonzalez. *Digital image processing*. eng. 4th ed. New York: Pearson, 2018. ISBN: 9781292223049.
- [37] Dongju Liu and Jian Yu. “Otsu method and K-means.” In: 1 (2009), pp. 344–349.
- [38] Christian Heumann, Michael Schomaker, et al. “Linear Regression.” In: *Introduction to Statistics and Data Analysis*. Springer, 2016, pp. 249–295.
- [39] Stéfan van der Walt. “Schö nberger JL, Nunez-Iglesias J, Boulogne F, Warner JD, Yager N, Gouillart E, Yu T, scikitimage contributors. 2014. scikit-image: image processing in python.” In: *PeerJ* 2 (), e453.
- [40] Anna M Karlberg et al. “Quantitative comparison of PET performance—Siemens Biograph mCT and mMR.” In: *EJNMMI physics* 3.1 (2016), pp. 1–14.
- [41] Doga Gürsoy et al. “TomoPy: a framework for the analysis of synchrotron tomographic data.” In: *Journal of synchrotron radiation* 21.5 (2014), pp. 1188–1193.

- [42] Y Vardi, L. A Shepp, and L Kaufman. "A Statistical Model for Positron Emission Tomography." eng. In: *Journal of the American Statistical Association* 80.389 (1985), pp. 8–20. ISSN: 0162-1459.
- [43] B M W Tsui et al. "Analysis of recorded image noise in nuclear medicine." eng. In: *Physics in medicine & biology* 26.5 (1981), pp. 883–902. ISSN: 0031-9155.
- [44] M S Rzeszotarski. "Counting statistics." eng. In: *Radiographics* 19.3 (1999), p. 765. ISSN: 0271-5333.
- [45] James D Brierley, Mary K Gospodarowicz, and Christian Wittekind. *TNM classification of malignant tumours*. John Wiley & Sons, 2017.
- [46] Douglas C Wolf. "Evaluation of the size, shape, and consistency of the liver." In: *Clinical Methods: The History, Physical, and Laboratory Examinations*. 3rd edition (1990).
- [47] *3D Slicer image computing platform*. URL: <https://www.slicer.org/>.
- [48] Andriy Fedorov et al. "3D Slicer as an image computing platform for the Quantitative Imaging Network." In: *Magnetic resonance imaging* 30.9 (2012), pp. 1323–1341.
- [49] J. D. Hunter. "Matplotlib: A 2D graphics environment." In: *Computing in Science & Engineering* 9.3 (2007), pp. 90–95. DOI: 10.1109/MCSE.2007.55.
- [50] Bum-Sahn Kim et al. "Usefulness of SUV ratio for differentiating benign from malignant focal thyroid lesions incidentally detected by F-18 FDG PET/CT: comparison with SUV analysis." In: *Journal of Korean Thyroid Association* 2.2 (2009), pp. 120–127.
- [51] Skipper Seabold and Josef Perktold. "statsmodels: Econometric and statistical modeling with python." In: *9th Python in Science Conference*. 2010.
- [52] Anthonin Reilhac et al. "Simulation-based evaluation of OSEM iterative reconstruction methods in dynamic brain PET studies." In: *Neuroimage* 39.1 (2008), pp. 359–368.
- [53] Jeroen Verhaeghe, Paul Gravel, and Andrew J Reader. "Task-oriented quantitative image reconstruction in emission tomography for single- and multi-subject studies." In: *Physics in Medicine & Biology* 55.23 (2010), p. 7263.
- [54] Claes N Ladefoged et al. "Dental artifacts in the head and neck region: implications for Dixon-based attenuation correction in PET/MR." In: *EJNMMI physics* 2.1 (2015), pp. 1–15.
- [55] Georg Schramm and Claes Nøhr Ladefoged. "Metal artifact correction strategies in MRI-based attenuation correction in PET/MRI." In: *BJR | Open* 1 (2019), p. 20190033.
- [56] Francois Jamar et al. "EANM/SNMMI guideline for 18F-FDG use in inflammation and infection." In: *Journal of Nuclear Medicine* 54.4 (2013), pp. 647–658.



# Appendix

## A.1 Patient dataset

The data protection official at UNN accepted the patient dataset to be used for this thesis, and claimed it exempt from permission from the regional ethics committee, as no personal data of the patient was accessed. The patient also gave his/hers informed written consent for the image data to be used for the purpose of this thesis. Before the data were accessed by the author, all patient information had been anonymized according to data protection recommendations in the Siemens Biograph mMR operator manual. The use of the PET/MR images was also filed in compliance with the hospital data protection regulations.

## A.2 Python code for running simulated tomography experiments and reconstructions

Here, the Python code written for running simulated tomography experiments and reconstructions is listed. An object oriented design was chosen. Properties of each class is documented in the respective classes.

### A.2.1 Class for simulating tomography experiments and do reconstruction

```

# Required libraries/packages/functions
import tomopy
import numpy as np
from skimage.filters import gaussian
from skimage.transform import radon

class Recon:
    """
    Class to reconstruct activity maps with two different attenuation
    maps.
    """
    def __init__(self, amap, umap, umap_art, filtering=True):
        """
        :param amap: Activity map. Must be an instance of the Amap class.
        :param umap: Attenuation map. Must be an instance of the Umap
        class.
        :param umap_art: Attenuation map with artifact. Must be an
        instance of the Umap class
        :param filtering: Boolean attribute to specify if Gauss filter
        should be applied.
        """
        self.pixel_spacing = 2 # Pixel spacing xy-direction [mm/pixel]
        self.filtering = filtering

        self.fwhm = 3 # Full width at half maximum for Gaussian filter
        self.nangles = 256 # Number of projection angles used for Radon
        # transform

        self.amap = amap
        self.umap = umap
        self.umap_art = umap_art

        # Initialization of sinograms
        self.sino_amap = None
        self.sino_umap = None
        self.sino_umap_art = None

        self.sino_nac = None
        self.sino_ac = None

```

```
self.sino_ac_art = None

# Initialization of reconstructed images
self.recon_org = None
self.recon_art = None

def run(self):
    """
    Method to run simulated tomography experiment.
    :return: Nothing
    """
    if self.filtering:
        self.gauss_filter(fwhm=self.fwhm)
        # print('Doing filter')

    self.sino_amap = self.create_3d_sinogram(self.amap)
    self.sino_umap = self.create_3d_sinogram(self.umap)
    self.sino_umap_art = self.create_3d_sinogram(self.umap_art)

    self.sino_nac = self.de_attenuate(self.sino_amap, self.sino_umap)
    self.sino_ac = self.apply_ac(self.sino_nac, self.sino_umap)
    self.sino_ac_art = self.apply_ac(self.sino_nac, self.sino_umap_art)

    self.recon_org = self.do_recon(self.sino_ac)
    self.recon_art = self.do_recon(self.sino_ac_art)

def gauss_filter(self, fwhm):
    """
    Method to apply Gaussian filtering to activity map and attenuation
    map(s).
    :param fwhm: Full width half maximum of Gaussian filter.
    :return: Nothing
    """
    self.amap = gaussian(self.amap, sigma=self.fwhm2sigma(fwhm),
                        preserve_range=True)
    self.umap = gaussian(self.umap, sigma=self.fwhm2sigma(fwhm),
                        preserve_range=True)
    self.umap_art = gaussian(self.umap_art,
                            sigma=self.fwhm2sigma(fwhm),
                            preserve_range=True)

def create_3d_sinogram(self, img_stack):
    """
    Computes slice-wise Radon transform of a 3-D stack of images.
```

```

        :param img_stack: image stack
        :return: stack of sinograms
        """
        sino_stack = np.zeros((img_stack.shape[0], img_stack.shape[1],
                               self.nangles))
        theta = np.linspace(0, 180, self.nangles, endpoint=False)
        for i in range(img_stack.shape[1]):
            sino_stack[:, i, :] = radon(img_stack[:, i, :], theta,
                                       circle=True, preserve_range=True)
        return sino_stack.T

def de_attenuate(self, sino_amap, sino_umap):
    """
    Method to de-attenuates sinogram. I.e, reversed attenuation
    correction to obtain non-attenuated sinograms.
    :param sino_amap: Sinograms of activity map
    :param sino_umap: Sinograms of attenuation map
    :return: Non-attenuated sinograms
    """
    nac_stack = np.zeros_like(sino_amap)
    for i in range(sino_amap.shape[1]):
        nac_stack[:, i, :] = np.exp(-sino_umap[:, i, :]) \
            * sino_amap[:, i, :]
    return nac_stack

def apply_ac(self, sino_amap, sino_umap):
    """
    Method to apply attenuation correction in the Radon space.
    :param sino_amap: Sinograms of activity map
    :param sino_umap: Sinograms of attenuation map
    :return: Attenuation corrected sinograms
    """
    ac_stack = np.zeros_like(sino_amap)
    for i in range(sino_amap.shape[1]):
        ac_stack[:, i, :] = np.exp(sino_umap[:, i, :]) \
            * sino_amap[:, i, :]
    return ac_stack

def do_recon(self, sino):
    """
    Reconstruct sinograms using OSEM algorithm from the Tomopy python
    package.
    :param sino: Sinograms to reconstruct
    :return: Reconstructed images

```



```
        """
        theta = tomopy.angles(sino.shape[0])
        recon = tomopy.recon(sino, theta, algorithm='osem', num_iter=12
                             , num_block=1)
        return recon

def fwhm2sigma(self, fwhm):
    """
    Method to compute the full width half maximum from the standard
    deviation of a Gaussian.
    :param fwhm: full width half maximum
    :return: standard deviation that corresponds to the specified full
            width half maximum.
    """
    sigma = (fwhm / self.pixel_spacing) / (np.sqrt(8 * np.log(2)))
    return sigma
```

## A.2.2 Class for activity maps

```
class Amap:
    """
    Class for activity maps. Can either create digital phantom, or take
    an existing activity map.
    """
    def __init__(self, size=None, lam_bg=None, amap=None, noise=False):
        """
        :param size: If specified, a digital phantom will be created.
        :param lam_bg: Mean background activity value (values will be
            drawn from a Poisson distribution)
        :param amap: Existing activity map
        :param noise: Boolean statement to decide if background noise
            should be present in the digital phantom.
        """
        self.lam_bg = lam_bg
        self.noise = noise

        if amap is not None:
            self.amap = amap
            self.size = self.amap.shape
        else:
            self.size = [size[0], size[1], size[2]]
            self.amap = np.zeros(self.size)
```

```

self.voi_mask = np.zeros_like(amap)

if noise:
    self.bg_noise = self.background_noise()
    self.amap += self.bg_noise

def make_sphere(self, center_point, r):
    """
    Method creates a spherical mask in a 3D Euclidean space of size
    [size x size x size]
    :param center_point: center point of sphere
    :param r: radius of sphere
    :return: boolean mask where pixel values = 1 where the sphere is
    """
    x0, y0, z0 = center_point
    x = np.arange(0, self.size[1])
    y = np.arange(0, self.size[0])
    z = np.arange(0, self.size[2])
    xx, yy, zz = np.meshgrid(x, y, z)
    mask = (xx - x0) ** 2 + (yy - y0) ** 2 + (zz - z0) ** 2 <= r ** 2
    return mask

def background_noise(self):
    """
    Adds background noise (Poisson noise) to a spherical region within
    the 3D euclidean space as defined by size [size x size x size].
    The spherical region has its center point at the center of the 3D
    space and radius size-1
    :return: poisson noise
    """
    mask = self.make_sphere(center_point=[self.size[1]/2,
                                           self.size[0]/2,
                                           self.size[2]/2],
                            r=self.size[0]/2-1)
    poisson_noise = np.random.poisson(lam=self.lam_bg,
                                      size=np.asarray(mask).shape)
    poisson_noise[(mask == False)] = 0
    return poisson_noise

def introduce_lesion(self, center_point, r, mean, const=True,
                    voi=False):
    """
    Creates a spherical "lesion" inside the 3D euclidean space

```

```
[size x size x size].
:param center_point: Center point of lesion
:param r: radius of lesion
:param mean: mean activity of lesion
:param const: Boolean statement to decide if lesion should have
              noise. If true, the activity in each pixel is
              drawn from a Poisson distribution; Poisson-(mean)
:param voi: Boolean statement. If true, the lesion is defined as a
           volume of interest and a mask is created to be able
           to calculate the activity within the lesion for
           analysis.
:return: Nothing (changes class attributes)
"""
mask = self.make_sphere(center_point, r)
if const: # If noise in the tumor is not allowed
    self.amap[(mask == 1)] = mean
else: # If we want noise in the tumor
    random_pool = np.random.poisson(lam=mean, size=np.sum(mask))
    self.amap[(mask == 1)] = np.random.choice(random_pool,
                                              np.sum(mask))

if voi:
    self.voi_mask = mask

def reset_amap(self):
    """
    Function to reset the activity map. If background noise is present,
    the activity map is reset to the noise.
    :return: Nothing
    """
    if self.noise:
        self.amap = np.copy(self.bg_noise)
        self.voi_mask = np.zeros_like(self.amap)
    else:
        self.amap = np.zeros(self.size)
        self.voi_mask = np.zeros_like(self.amap)

def slice_z(self, slc_center, slc_width):
    """
    Method to select slices in z-direction: selected slices =
    slc_center +/- slc_width.
    :param slc_center: Center z-slice
    :param slc_width: width from center slice
    :return: Nothing
    """
```

```

"""
slc_start = int(slc_center - slc_width)
slc_stop = int(slc_center + slc_width + 1)
self.amap = self.amap[:, slc_start:slc_stop, :]
self.voi_mask = self.voi_mask[:, slc_start:slc_stop, :]

```

### A.2.3 Class for attenuation maps

```

class Umap:
    """
    Class for activity maps. Can either create digital phantom, or take
    an existing activity map.
    """
    def __init__(self, size=None, umap=None):
        self.size = size
        if umap is not None:
            self.umap = umap
            self.size = self.umap.shape
        else:
            self.umap = np.zeros(self.size)

    def make_sphere(self, center_point, r):
        """
        Method creates a spherical mask in a 3D Euclidean space of size
        [size x size x size]
        :param center_point: center point of sphere
        :param r: radius of sphere
        :return: boolean mask where pixel values = 1 where the sphere is
        """
        x0, y0, z0 = center_point
        x = np.arange(0, self.size[1])
        y = np.arange(0, self.size[0])
        z = np.arange(0, self.size[2])
        xx, yy, zz = np.meshgrid(x, y, z)
        mask = (xx - x0) ** 2 + (yy - y0) ** 2 + (zz - z0) ** 2 <= r ** 2
        return mask

    def introduce_attenuating_object(self, center_point, r, uval):
        """
        Method to introduce a spherical attenuating object in the
        attenuation map.
        :param center_point: center point of attenuating object
        :param r: radius of attenuating object

```

```

        :param uval: Linear attenuation coefficient of the attenuating
        object.
        :return: Nothing
        """
        mask = self.make_sphere(center_point, r)
        self.umap[(mask == 1)] = uval

def introduce_artifact(self, center_point, r, uval):
    """
    Introduces a spherical artifact to the attenuation map.
    The artifact attenuation map is a separate attribute within the
    class.
    :param center_point: Center point of artifact
    :param r: radius of artifact
    :param uval: linear attenuation coefficient of artifact volume
    :return: Nothing
    """
    mask = self.make_sphere(center_point, r)
    self.umap = np.copy(self.umap)
    self.umap[(mask == 1)] = uval

def slice_z(self, slc_center, slc_width):
    """
    Method to select slices in z-direction: selected slices =
    slc_center +/- slc_width.
    :param slc_center: Center z-slice
    :param slc_width: width from center slice
    :return: Nothing
    """
    slc_start = int(slc_center - slc_width)
    slc_stop = int(slc_center + slc_width + 1)
    self.umap = self.umap[:, slc_start:slc_stop, :]

```

### A.3 Python code for correction method

The Python code for the proposed correction method is given below.

```

# Required packages/libraries/functions
import numpy as np
from skimage.filters import threshold_otsu

def correction_method(attenuation_map, oop_images):

```

```

"""
Proposed correction method for correcting voxels in the liver of an
attenuation map that has been falsely assigned the attenuation value of
lung tissue

:param attenuation_map: Attenuation map with lung/liver
misclassification
:param oop_images: Opposed-phase Dixon images used to to obtain the
attenuation map. NB! Must be registered and resampled to the
attenuation map for method to work.
:return: Corrected attenuation map
"""
mask = np.zeros_like(imgs_umap) # Initialize mask

# Create boolean mask. Mask=1 at all locations where the attenuation
# map has the attenuation value of lung tissue. Mask=0 elsewhere.
mask[imgs_umap == 224] = 1

# Find corresponding voxels in the opposed-phase image.
voi = imgs_oop[mask == 1]

# Find best threshold to separate lung/soft tissue in opposed phase
# image
thresh = threshold_otsu(voi, nbins=256)

# Create correction mask containing all voxels in the opposed-phase
# image that are >= obtained threshold
correction_mask = (imgs_oop >= thresh) & (mask == 1)

# Change all voxels in the attenuation map that =1 in the correction
# mask. Assign soft tissue attenuation values.
imgs_umap[correction_mask == 1] = 1000
return imgs_umap

```



